EMI-GCN: a hybrid model for real-time monitoring of multiple bolt looseness using electromechanical impedance and graph convolutional networks

OPEN ACCESS
IOP Publishing
Smart Materials and Structures
Smart Mater. Struct. **30** (2021) 035032 (20pp)
https://doi.org/10.1088/1361-665X/abe292

EMI-GCN: a hybrid model for real-time monitoring of multiple bolt looseness using electromechanical impedance and graph convolutional networks

Lu Zhou[1,2], Si-Xin Chen[1,2], Yi-Qing Ni[1,2] and Alex Wai-Hing Choy[3]

[1] Hong Kong Branch of National Transit Electrification and Automation Engineering Technology Research Center, Hung Hom, Kowloon, Hong Kong Special Administrative Region of China
[2] Department of Civil and Environmental Engineering, The Hong Kong Polytechnic University, Hung Hom, Kowloon, Hong Kong Special Administrative Region of China
[3] Industrial Centre, The Hong Kong Polytechnic University, Hung Hom, Kowloon, Hong Kong Special Administrative Region of China

E-mail: lu.lz.zhou@polyu.edu.hk

Received 16 November 2020, revised 10 January 2021
Accepted for publication 2 February 2021
Published 18 February 2021

Abstract

Electro-mechanical impedance (EMI) has been proved as an effective non-destructive evaluation indicator in monitoring the looseness of bolted joints. Yet due to the complex electro-mechanical coupling mechanism, EMI-based methods in most cases are considered as qualitative approaches and are only applicable for single-bolt monitoring. These issues limit practical applications of EMI-based methods in industrial and transportation sectors where real-time and reliable monitoring of multiple bolted joints in a localized area is desired. Previous research efforts have integrated various machine learning (ML) algorithms in EMI-based monitoring to enable quantitative diagnosis, but only one-to-one (single sensor single bolt) case was considered, and the EMI–ML integrations are basically unnatural and ingenious by learning the EMI measurements from isolated sensors. This paper presents a novel EMI-based bolt looseness monitoring method incorporating both physical mechanism (acoustic attenuation) and data-driven analysis, by implementing a lead zirconate titanate (PZT) sensor network and a built-in graph convolutional network (GCN) model. The GCN model is constructed in such a way that the structure of the PZT network is fully represented, with the sensor-bolt distance and sweeping frequency encoded in the propagation function. The proposed method takes into account not only the EMI signature but also the relationship between the sensing nodes and the bolted joints and can quantitatively infer the torque loss of multiple bolts through node-level outputs. A proof-of-concept experiment was conducted on a twin-bolt plate, and results show that the proposed method outperforms other baseline models either without a graph network structure or does not consider sensor-bolt distance. The developed hybrid model provides new thinking in interpreting sensor networks which are widely adopted

in structural health monitoring, and the approach is expected to be applicable in practical scenarios such as rail insulated joints and aircraft wings where bolt joints are clustered.

Keywords: electro-mechanical impedance, structural health monitoring, graph convolutional network, machine learning, sensor network, bolt looseness, piezoelectric transducer

(Some figures may appear in colour only in the online journal)

1. Introduction

Being the most widely used parts in industrial and transportation areas connecting mechanical assemblies, bolted joints are vulnerable to various types of damages including cracks, corrosions, and looseness due to long-term service for transferring heavy loads and exposure to the harsh operating environment. Among all damage types, bolt looseness is the most common failure. The causes of bolt looseness can be external forces, vibrations or even excessive axial force applied on the bolt itself. The bolt looseness can be directly and manually measured and controlled by a torque wrench. Despite the simplicity and low-cost, manual inspections are often inaccurate since the majority of the applied torque is used to counter the friction and only a small portion is for bolt spinning [1]. Direct inspection as such is inapplicable in the scenarios where bolts are hidden inside the structure and cannot be directly accessed. What is more important, to obtain continuous loading information of in-service bolts, online long-term monitoring of bolts is desired, especially in the aviation and railway sector where loosening of bolts in operating trains or aircraft can be extremely vital.

In recognition of the problem, structural health monitoring (SHM) techniques have been investigated and applied for online diagnosis of bolt looseness. Structural sensors are typical options for loading state monitoring of bolts. With strain gauges either implemented on the target bolt or fabricated as smart washers, the axial force can be determined, and the applied torque can be subsequently derived with existing contact theories [2]; dynamic behavior of the monitored bolts is also an efficient index to diagnose the structural variations. With accelerometers implemented on the host structure, output responses subject to impact [3, 4], heavy loadings [5, 6] or laser excitation [7] can be acquired for further condition assessment; smart materials such as optical fibers have also been utilized for monitoring of bolt looseness. A normal single-mode fiber liner incorporated with the optical time-domain reflectometer enables the monitoring of multiple bolted joints at the same time [8], but the applicability in practical applications is yet to be proved with further *in-situ* investigations.

Ultrasound, bearing the merits of truly non-invasive, high-sensitivity and environment-friendly, has been systematically studied and extensively utilized in many SHM real applications. Ultrasonic testing comes in different forms, among which ultrasonic guided waves (UGWs) is a mature SHM technique in inspecting and monitoring the structural integrity of components at multi-scale sizes from machine elements to civil infrastructure, including the looseness of bolted joints [9, 10]. Apart from guided waves, ultrasonic bulk waves can also be utilized for characterizing the looseness of bolted joints. The loosening of a bolted joint indicates a reduction of contact pressure, which can be detected using an ultrasonic reflectometry approach. This approach has literally been used in railway engineering investigating various aspects including wheel-rail contacts [11, 12] and insulated rail joints. The philosophy of both guided wave- and bulk wave-based methods for bolted joint monitoring are based on waveform analysis of received ultrasonic signals, which are dominated by not only material properties of the propagating media, but more importantly, the geometry of the host structure, hence adding difficulty in signal processing for geometrically complicated structures. For a specific host structure to be monitored with UGW-based approaches, the dispersion behavior needs to be investigated first [13], while the ultrasonic reflectometry approach highly relies on the macro profile and micro appearance (surface roughness) of the contacting interfaces.

As a special type of ultrasonic inspection technique, the electro-mechanical impedance (EMI)-based methods, by contrast, do not need specific interpretation of ultrasound waveforms [14, 15], but rather identify the structural change by measuring the impedance of the entire electro-mechanical couple composed of sensors and the host structure, and have drawn growing attention in SHM applications, including monitoring of structural damages [16–19], axial stress variation [20], composite plates [21, 22] as well as load change of pin-connected and bolted joint-connected structures [23, 24]. However, the complicated electro-mechanical coupling mechanism limits the applicability of the EMI-based monitoring methods which, in most cases, are treated as a qualitative way to indicate the existence of structural variation and are only applicable in single bolt monitoring. The root cause of the limitation is that EMI measurements contain massive convoluted and entangled information of the whole structure and are influenced by boundary conditions, material properties, sensor-bolt distance, ambient temperature as well as structural integrity. It is tricky to sort out the contributions from all potential factors with purely analytical inference, making it difficult to manually correspond a feature or an index to a structural change occurred at a specific position. As EMI measurements reflect structural dynamic responses of the host structure subject to a series of ultrasonic excitations, there have been quite a few studies on analytical modelling of the electro-mechanical couple [25, 26]. Yet the analyzed objective is either a Timoshenko beam or a cube, and it is practically impossible to achieve a federation of explicit governing equations that

quantitatively characterize the contribution of a local structural variation to the change of the mechanical impedance, with all factors well considered.

In this regard, seeking aid from machine learning (ML) is a reasonable alternative in automatically extracting the features of interest out of the 'chaotic complexity' masked by the simple appearance of EMI curves. State-of-the-art ML techniques, especially neural networks (NNs) have been applied in many research efforts for EMI-based damage detection and bolt looseness monitoring [27–34]. For example, Zhu *et al* proposed a novel signature extraction method and achieve damage localization by a modified probability-weighted algorithm [27]. Probability was also considered in [28], where a probabilistic NN was developed and could be trained with minimal data. With the development of convolutional neural networks (CNNs) in recent years, it has been combined with EMI for damage detection [29, 30]. The emergent capsule NN has also been utilized for bolt early looseness detection based on percussion-induced sound [31]. There were studies attempting to select the most sensitive frequency range to the expected structural damage. Min *et al* [32] utilized the NN approach to automatically select the optimal frequency range in the EMI method. The governing frequency components were validated by observing the internal weights and biases in the NN. This study was extended in [33] to estimate a range of damage information, such as damage type and severity simultaneously. In the process of damage identification [34], added a sparse regularization so that the number of measured resonance frequency shifts for identification can be very limited. These studies are innovative in various aspects, but the applications are still limited within the single sensor-single damage/bolt loosening scenarios, and the sensor-bolt distance which ought to have significant influence according to the physical nature of ultrasonic approaches, is hardly considered in previous research. Moreover, the hand-crafted features in the studies may not fully reveal the information of structural changes and thus influence the performance of the trained model, and the models trained are usually classifiers, which cannot identify any scenario out of the pre-determined classes.

In light of the challenges and existing limitations of EMI-based monitoring methods, in the present study, we adopt a sensor network comprised of multiple PZT sensing elements and propose a novel ML paradigm aiming at monitoring the looseness of multiple bolted joints. Enlightened by the latest research work in computer science, we introduce the concept of graph/network learning to EMI-based monitoring, and the torque losses of multiple bolted joints are expected to be jointly determined with the graph/network learning model and the PZT sensor network. The target is achieved by firstly abstracting the PZT sensors and target bolts into a graph that fully describes the overall layout. Subsequently, a hybrid EMI-graph convolutional network (GCN) model which not only takes in the EMI signature of interest but also the relationship between sensors and bolts is proposed. The torque losses of all monitored bolts can be determined through node-level outputs of the trained EMI-GCN model while retaining the graph structure throughout the learning process. To the authors' knowledge, it is the first-time graph learning is introduced into the realm of SHM, in which both sensor networks and clustered bolted joints are widely confronted. Moreover, distinguished from conventional GCN models that are fully data-driven, the formulated hybrid EMI-GCN model in this study also incorporates acoustic attenuation nature by encoding the sensor-bolt distance and sweeping frequency in the forward propagation process. A proof-of-concept experiment and comparison with conventional ML methods are carried out to demonstrate the effectiveness and outperformance of the proposed method.

The rest of the paper is organized as follows. Section 2 presents the principles of EMI-based monitoring and acoustic attenuation. The establishment of the hybrid EMI-GCN model is delivered in section 3. The proof-of-concept experiment with results and performance comparison with baseline models are introduced in section 4. Conclusions and future work are elaborated in section 5.

2. Principles of EMI-based monitoring and proposal of questions

2.1. EMI-based monitoring technique

Analogous to other ultrasonic monitoring techniques, the EMI-based methods rely on the piezoelectric and inverse piezoelectric effect, i.e. the conversion between electrical energy and mechanical energy of piezoelectric materials (e.g. PZT), but from a different perspective. When actuating the PZT sensor implemented on the host structure of interest with cyclic electrical excitations, a localized electrical–mechanical (EM) coupling system is formed between the sensor and the host structure, which vibrates in response to the external vibrations. The passing current through the sensor is altered by the structural response of the EM system and can be measured using an impedance analyzer, in the form of EMI. By sweeping the excitation frequency, a series of EMI can be measured, corresponding to structural responses that contain condition information of the host structure. Any change (cracks, fracture, bolt looseness, etc) in the host structure would be reflected in the structural dynamic responses and accordingly the EMI measurements, making EMI-based monitoring applicable [35]. The most widely used analytical model is the one-dimensional (1D) EMI model proposed by Liang *et al* in [36] which treats the host structure as a single-degree-of-freedom mass-spring system coupled with a PZT patch, as shown in figure 1. It has been revealed in [37] that the electrical admittance $Y_{\mathrm{e}}(\omega)$, inverse of the electrical impedance, has relationship with the mechanical impedance of the host structure, $Z_{\mathrm{s}}(\omega)$ and that of the PZT patch, $Z_{\mathrm{a}}(\omega)$ under external excitation with frequency ω:

$$Y_{\mathrm{e}}(\omega) = j\omega c\left(\bar{\varepsilon}_{33}^{T} - \frac{Z_{\mathrm{s}}(\omega)}{Z_{\mathrm{s}}(\omega)+Z_{\mathrm{a}}(\omega)} d_{3x}^{2} Y_{xx}^{E}\right) \tag{1}$$

where c, $\bar{\varepsilon}_{33}^{T}$, d_{3x}, and Y_{xx}^{E} are the geometry constant, complex dielectric constant, PZT coupling constant, and complex Young's modulus of the PZT patch at zero stress, respectively.

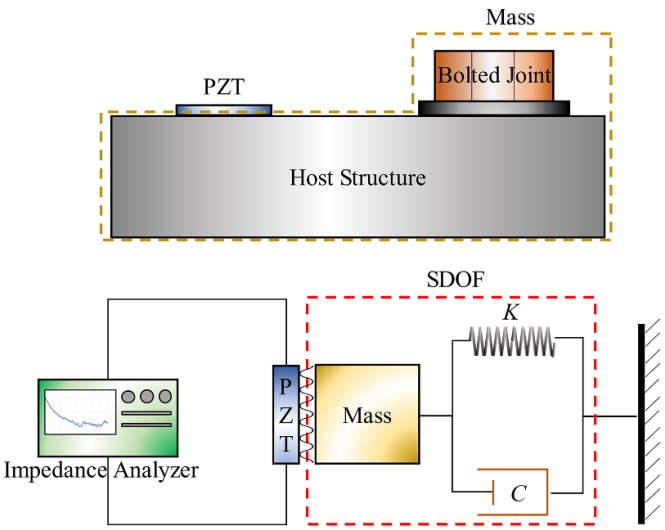

Figure 1. 1D EMI model.

Further analytical research on 2D and 3D models can be found in [25, 38] for certain PZT wafers and host structures. Specifically, a very recent article [39] proposed the three-dimensional modelling method to simulate the PZT active sensing and, consequently, monitor the looseness of bolted connections.

It should be noted that the 1D model in most cases serves as a rough validator, and all existing 2D and 3D analytical models are established on simple structures such as a beam, a plate, etc. In most practical monitoring scenarios including bolted joint mechanisms, however, these analytical models can only provide limited references on potentially influencing factors, since the structures are too complicated to derive an analytical relationship, and the EMI measurements have to be obtained through an experimental device (impedance analyzer). Ideally, if all environmental influences and material uncertainties are neglected, in principal greater deviation from the baseline EMI measurements indicates larger structural change. To quantify the deviation, four statistical metrics are generally utilized [40], including root mean square deviation, mean absolute percentage deviation, covariance (Cov) as well as correlation coefficient (CC).

As stated in the introduction, in reality, the environmental influences, nevertheless, can hardly be overlooked and the conventional quantification metrics always need to be accompanied by ML methods to be fully functioning. On the other hand, in all previous EMI-based monitoring research, only one-on-one (single sensor single bolt) cases were mainly investigated. From an intuitive perspective, introducing more sensors in a monitoring scenario should bring more information [41], as what is adopted in UGW-based monitoring [42]. But unlike UGW-based methods that follow a clear clue of wave interpretation (dispersion curve, nonlinear factor, etc.), how to incorporate a similar sensor array or network into EMI-based monitoring is challenging. In face of this, we present new thinking to encode the sensor network into the ML framework with its core philosophy detailed in section 3.

2.2. Attenuation of ultrasound

Although the EMI-based monitoring method measures the dynamic response of the whole structure, the diffusion behavior of the mechanical vibrations is analogous to the propagation mechanism of ultrasound waves which are essentially mechanical vibrations as well, and the sensing process can be regarded as information transmitted from the spot where the structural change (bolt loosening) to the PZT patch in the form of EMI, as illustrated in figure 2. In this sense, the acoustic attenuation should cast significant influence.

The acoustic attenuation is contributed by two parts: absorption and scattering. Absorption refers to the phenomenon of energy conversion from mechanical vibrations to heat, as the vibrating particles in the host structure need to overcome resistive frictional forces when ultrasound propagates; scattering occurs when ultrasonic sound waves encounter inhomogeneities (material bulk, density change, etc) in the host material structure, and the signal is partially reflected as well as being refracted at the boundary of inhomogeneity. Excluding material property factors, there are two main terms that dominate the attenuation level: distance and frequency. The longer the propagation distance is, the more frictional forces and material inhomogeneities will be encountered, leading to increases in absorption and scattering correspondingly. On the other hand, when the frequency of the sound waves increases, the particles vibrate faster, increasing the frictional forces and subsequently the absorption. Higher frequency also indicates shorter wavelength, and it becomes easier to scatter the sound waves, because the relative size of the inhomogeneities increases comparing to the wavelength.

Yet in previous studies on EMI-based monitoring, these two terms are seldom considered. However, in practical applications, the EMI-based technique is deemed to be a localized technique, which implies the distance does matter significantly. By understanding the influence of sensor-bolt distance in detail, we are able to know how much of an EMI deviation is contributed by the loosening of a closer bolt and how much is contributed by the loosening of one further away in a multi-bolt structure. Min *et al* took the sensor-bolt distance into account by normalizing the EMI measurement with a coefficient equivalent to the reciprocal of the distance. Despite their inspiring work, the coefficient in [33] lacks theoretical support and such a hypothesis literally fails when it comes to a smart EMI washer [43] case where the sensor-bolt distance becomes zero.

The EMI-based monitoring involves polarization of PZT sensors as well as the host structure which is made of lossy media (steel) in which a significant amount of wave energy is attenuated in the propagating process. As proposed in [44], the frequency-dependent attenuation of ultrasonic sound waves $\boldsymbol{u}(\boldsymbol{r})$ in a lossy medium can be described using a fractional constitutive model using a modified stochastic wave equation as:

$$\nabla^2\boldsymbol{u}(\boldsymbol{r}) - \frac{1}{c_0^2}\frac{\partial^2\boldsymbol{u}(\boldsymbol{r})}{\partial t^2} + \tau_\sigma^\alpha\frac{\partial^\alpha}{\partial t^\alpha}\nabla^2\boldsymbol{u}(\boldsymbol{r}) - \frac{\tau_\varepsilon^\beta}{c_0^2}\frac{\partial^{\beta+2}\boldsymbol{u}(\boldsymbol{r})}{\partial t^{\beta+2}} = 0 \tag{2}$$

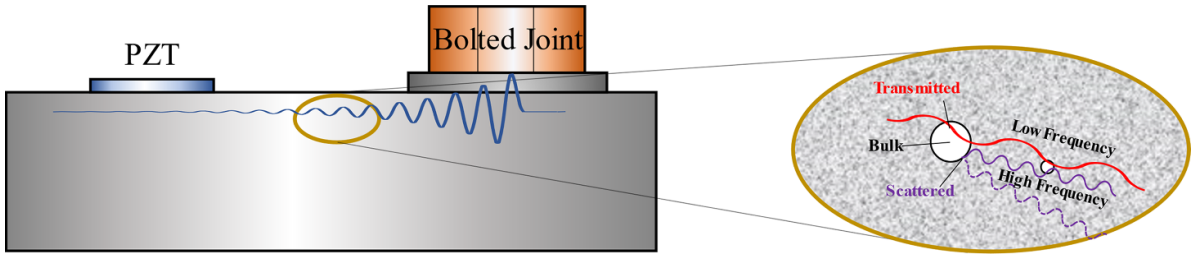

Figure 2. Structural vibration propagated from bolt to sensor in EMI monitoring.

where ∇^2 is the Laplace operator given by $\nabla^2 = \partial^2/\partial x^2 + \partial^2/\partial y^2 + \partial^2/\partial z^2$ in a three-dimensional Cartesian coordinate. The first two terms in equation (2) represents the conventional stochastic wave equation, and the last two terms contain higher-order spatial and fractional derivatives. The amplitude $A(r)$ of $\boldsymbol{u}(\boldsymbol{r})$ represents the sound energy of the ultrasonic vibrations, and therefore directly corresponds to the signal strength in EMI-based monitoring. The amplitude follows a power law with respect to both frequency ω (in MHz unit) and propagation distance Δd (in m unit) and is given by:

$$A(r+\Delta d) = A(r)\,\mathrm{e}^{-\delta_0 \omega^{\eta} \Delta d} \tag{3}$$

where δ_0 and η are real non-negative material parameters.

The power-law frequency-dependent attenuation of sound waves has been validated through many experiments [45–47]. As one of the highlights in this study, we are aiming to propose a more reasonable rule following this attenuation law, and to encode the influence of both distance and frequency into the proposed ML framework to construct a novel physical-data driven hybrid learning model. Details of the model construction are presented in the next section.

3. Establishment of EMI-GCN model

3.1. From sensor network to graph

Consider a cluster of bolts surrounded by several randomly and locally distributed PZT sensors in an EMI-based monitoring scenario, as shown in figure 3 (for illustration convenient purpose, only a limited number of bolts and sensors are plotted). For each measurement taken from a sensor, a line is drawn from each of the bolts to that sensor, indicating that each EMI curve contains residual torque information of all neighboring bolts. By taking EMI readings from all sensors, a complete undirected bipartite graph is constructed with all sensors and bolts serving as nodes of the graph, and all connecting lines serving as edges. A bipartite graph is a graph whose nodes can be divided into two independent and disjoint sets $\boldsymbol{B}$ and $\boldsymbol{S}$ such that every edge connects an element in $\boldsymbol{B}$ to an element in $\boldsymbol{S}$; 'complete' means each of the element in $\boldsymbol{B}$ is connected to all elements in $\boldsymbol{S}$, and vice versa; 'undirected' means all edge do not have directions, since there is no concept of pitch-catch in EMI monitoring.

In graph theory, a graph $\mathbf{G}$ is uniquely defined by three features: nodes, edges and the graph structure. The graph structure is typically represented in the form of an $n \times n$ adjacency matrix $\boldsymbol{A}$. Under normal circumstances, the element of $\boldsymbol{A}$ is determined in the following manner:

$$\begin{cases} A_{ij} = 1, & \text{if there is a connection from node } i \text{ to node } j \\ A_{ij} = 0, & \text{otherwise} \end{cases}. \tag{4}$$

Taking the constructed graph in figure 3 as an example, if we number all sensor nodes and bolt nodes in order, its adjacency matrix can be readily determined, as shown in figure 4. For an undirected graph, the adjacency matrix is always symmetric.

Therefore, generally speaking, a graph $\mathbf{G}$ can be denoted as $\mathbf{G} = (\mathbf{V}, \mathbf{E}, A)$, where $\mathbf{V}$ is the set of nodes (vertices), $\mathbf{E}$ is the set of edges [48], while v_i denotes a vertex and $e_{i,j} = (v_i, v_j) \in \mathbf{E}$ denotes an edge. Apart from the graph structure, the core information of a graph is also associated with node attributes, represented by a feature matrix $\boldsymbol{X} \in \boldsymbol{R}^{n \times d_0}$, in which $\boldsymbol{x}_i \in \boldsymbol{R}^{d_0}$ is the feature vector of node v_i, and a label matrix $\boldsymbol{Y} \in \boldsymbol{R}^{n \times d_y}$, in which $\boldsymbol{y}_i \in \boldsymbol{R}^{d_y}$ is the label vector of node v_i, d_0 and d_y being the dimensions. For referencing convenient purpose, notations of a graph are summarized in table 1.

Up to this step, we have almost fully abstracted the PZT sensor network together with the target bolted joints into a uniquely defined graph as a mathematical representation. Distinguished from conventional EMI methods that look into the metrics separately, our thinking is to propose an ML paradigm that learns the entire graph containing both EMI measurements and their relationships including position information. To achieve this target, the concept of graph neural networks (GNNs), or more specifically, GCNs, which were widely applied in other disciplinaries for social network recognition [49], traffic flow prediction [50] and protein-interaction network identification [51], are utilized in this study.

3.2. GCNs

Many ML tasks, which once heavily relied on handcrafted feature engineering to extract informative feature sets, has recently been revolutionized by various end-to-end deep learning paradigms. Deep learning can extract latent representation from Euclidean data (e.g. images, text, and video). For example, an image can be represented as a regular grid in the Euclidean space. Correspondingly, a CNN model is able to exploit the shift-invariance, local connectivity, and compositionality of image data. As a result, CNNs can extract local meaning features that are shared with the entire datasets for

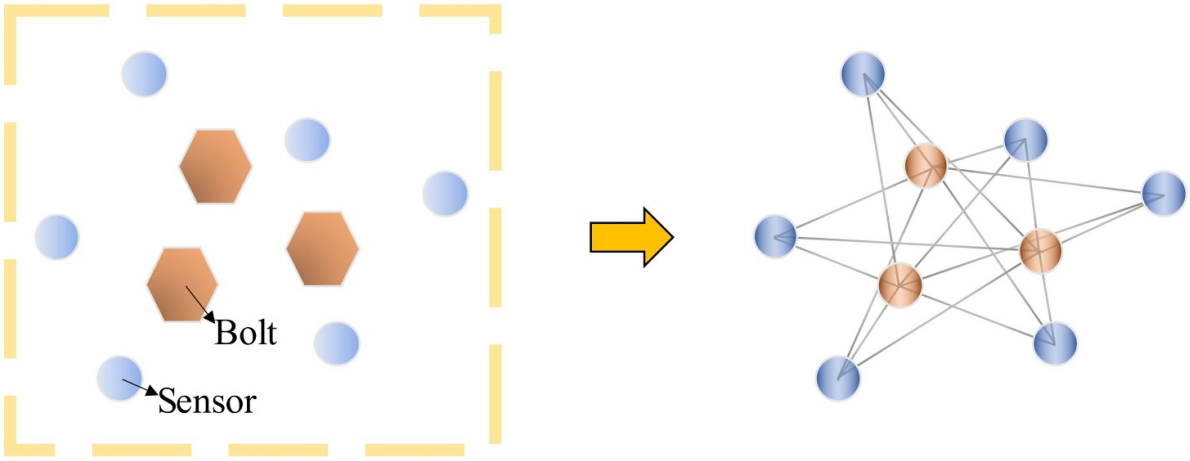

Figure 3. PZT sensor network for bolt monitoring and its corresponding graph.

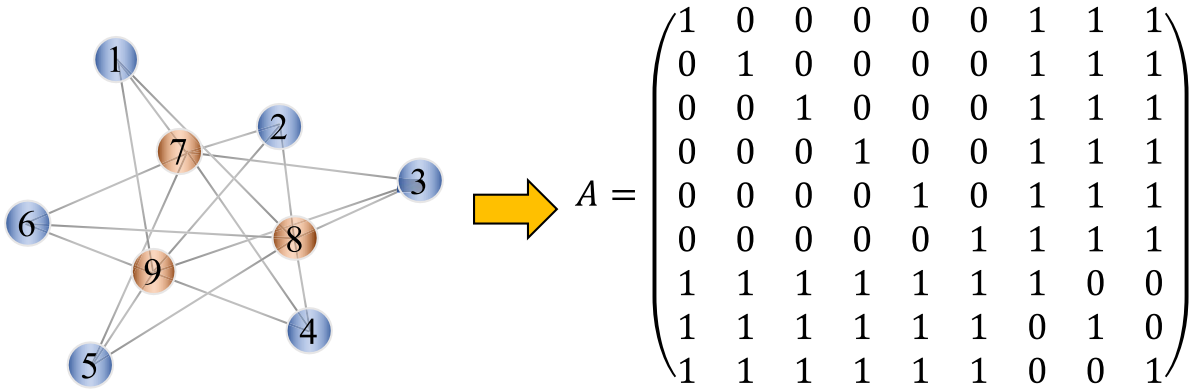

Figure 4. Sensor-bolt graph with numbered nodes.

Table 1. Commonly used notations.

Notations	Meaning
$\mathbf{V}$	The set of nodes
v_i	A node $v_i \in \mathbf{V}$
$\mathbf{E}$	The set of edges
$e_{i,j}$	An edge $e_{i,j} \in \mathbf{E}$
$\mathbf{N}(v_i)$	The set of neighbors of v_i
$\boldsymbol{A}$	Adjacency matrix
$a_{i,j}$	The connection intensity between v_i and v_j
$\boldsymbol{X}$	Feature matrix
$\boldsymbol{x}_{\mathrm{i}}$	The feature vector of node v_i
$\boldsymbol{Y}$	Label matrix
$\boldsymbol{y}_i$	The label vector of node v_i

various image analysis tasks. CNNs are highly useful in learning normal images, but when it comes to structured data, manifested as a graph, conventional CNNs may not apply. As mentioned in section 3.1, we can describe a graph by (weighted or directly) adjacency matrix and feature matrix. However, each graph has a variable size of unordered nodes and each node in a graph has a different number of neighbors. Furthermore, each node may be related to others via some complex linkage information. Therefore, important operations like convolutions are not directly applicable to the graph domain anymore.

To handle the complexity of graph data, new generations and definitions for important operations have been rapidly developed over the past few years. An ideal deep learning model for graph should handle the following tasks:

- Summarize the information contained in the nodes, which can be achieved by NNs.
- Propagate the information throughout the whole graph, which involves graph theory.

Figure 5 illustrates how a simple graph convolution is inspired by a standard 2D convolution in CNNs and GNNs respectively. The 2D convolution takes a weighted average of pixel values of the red node along with its neighbors, which are ordered and have a fixed size. Correspondingly, to get a hidden representation of the red node, a simple graph convolution takes the average (or weighted average) value of node features of the red node along with its neighbors. Different from image data, the neighbors of a node are unordered and varying in size.

As a representative type of GNNs, GCNs generalize the operation of convolution from traditional data (images or grids) to graph data. With the graph structure and node features as inputs, GCNs learn to conduct node-level regression

(a) (b)

Figure 5. Grid convolution VS graph convolution: (a) grid convolution; (b) graph convolution.

or classification. For one node v_i, by aggregating its own features $\boldsymbol{x}_i$ and neighbors' features $\boldsymbol{x}_j$, where $j \in \mathbf{N}(\mathrm{v}_i)$, its latent representation can be obtained.

Technically, a layer-wise propagation can be described as:

$$O^{(k)} = \sigma\left(AO^{(k-1)}W^{(k)}\right) \tag{5}$$

where $O^{(k)}$ represents the feature matrix containing the feature of each node after the kth layer; at the beginning, $O^{(0)} = X$; $W^{(k)}$ is the weight matrix for the kth graph convolution layer; A is the adjacency matrix; and $\sigma()$ is the non-linear activation function (e.g. ReLU).

Given the degree matrix D, in practice, a variant propagation rule introduced is:

$$O^{(k)} = \sigma\left(D^{-\frac{1}{2}}AD^{\frac{1}{2}}O^{(k-1)}W^{(k)}\right). \tag{6}$$

This operation symmetrically normalizes A and prevent the feature vectors from scale explosion.

In our study, we obtained a weighted adjacency matrix according to the distance between sensor and bolt. In addition, we normalize A in a slightly different way. More details are explained in section 3.3.

The outputs of GCNs can focus on different graph analytics tasks. GCN model is able to conduct node-level regression and classification, and it also can generate edge-level outputs or graph-level outputs by integrating node representations of pairwise nodes or the whole graph, respectively.

In this study, we consider the problem of predicting the labels of some nodes (bolts), where information is only available for some other nodes (sensors). This problem can be framed as graph-based semi-supervised learning.

In this case, a label matrix $\boldsymbol{Y} \in \boldsymbol{R}^{n\times d_y}$ is also available, in which $\boldsymbol{y}_i \in \boldsymbol{R}^{d_y}$ is the label vector of node v_i. The parameters of the network can be learned by comparing the output of the last layer $O^{(L)}$ and the label matrix $\boldsymbol{y}$. More details are provided in section 3.3.

3.3. Construction of EMI-GCN model

3.3.1. Definition of matrix elements. With the GCN tool and the graph abstracted in the EMI network scenario, our next step is to bridge the gap and fabricate a special GCN (EMI-GCN) model targeted for our case with the acoustic attenuation considered in the meantime. Prior to that, the feature and label of the graph need to be defined in the first place. Hereby we treat the bolt nodes and the sensor nodes as the same type of nodes, although for illustration clear they are colored differently in figures. Considering EMI-based bolt looseness monitoring is to measure the torque loss of the bolts based on deviations of quantifying metrics of EMI signatures, the feature of each sensor should be the metric deviations from reference (data collected from the fully fastened state), and the feature of each bolt is defined as zero, since no EMI measurement is taken from the bolt. Correspondingly, the label of each bolt should be the torque loss, and the label of each sensor does not need to be defined since it is trivial being by-products of the GCNs learning process.

Following the definition in section 2, the EMI-GCN model is formulated to learn a function of features on a graph which takes the following as input:

- A $n \times d_0$ matrix X where $\boldsymbol{x}_i$ is the feature for each v_i; n is the number of nodes, including n_b bolt nodes and n_s sensor nodes; d_0 is the number of input features.
- An adjacency matrix A that describes the graph structure in a matrix form.

The adjacency matrix A is already determined in section 3.1. As for the feature matrix X, we choose correlation coefficient deviation (CCD) as the quantifying metric of EMI measurements. Note that both the admittance function $Y(\omega)$ and the measured impedance in equation (1) are complex numbers and the calculation of the metrics usually only considers the real part, which is found more sensitive to the structural damage than the imaginary part [52]. For a specific range of frequency $\omega_1 \sim \omega_2$, the CC is calculated as:

$$CC_{\omega 1,\omega 2} = \frac{1}{(\omega_2-\omega_1)}\sum_{i=\omega_1}^{\omega_2}\frac{\left[\mathrm{Re}\left(Z_0(i)\right)-\bar{Z}_0\right]\left[\mathrm{Re}\left(Z_1(i)\right)-\bar{Z}_1\right]}{\sigma_{z_0}\sigma_{z_1}}$$
$$CCD_{\omega 1,\omega 2} = 1 - CC_{\omega 1,\omega 2} \tag{7}$$

where Z_1 is the impedance signature in the condition of interest while Z_0 is the reference; $\bar{Z}_0$ and $\bar{Z}_1$ are the average values in $\omega 1 \sim \omega 2$ for two signatures respectively; and σ_{z_0} and σ_{z_1} are the standard deviations. For fully fastened bolts, the CC is 1 and the CCD is 0.

It is discovered in [33] with the scanning frequency range from 10 kHz to 100 kHz, EMI signatures under specific frequency range (60–80 kHz) were more responsive to the structural change (crack), whereas those under 10–40 kHz, and 90–100 kHz were more responsive to the changes in a boundary condition for their case. Since the boundary condition, scanning frequency and host structure are different case by case, we need to find the frequency range sensitive to bolt loosening in this study through the learning process. To achieve this, for each node, the EMI spectrum with exciting frequency starting from ω_s and ending at ω_e is divided into d_0 sub-ranges and the CCDs are calculated piecewisely to formulate the feature matrix:

$$\boldsymbol{x}_i = \left[CCD_{\omega_s,\omega_s+\frac{\omega_e-\omega_s}{d_0}}, \ldots, CCD_{\omega_e-\frac{\omega_e-\omega_s}{d_0},\omega_e}\right]$$
$$X = \left[\ 0, \quad \cdots, \quad 0_{n_b}, \quad \boldsymbol{x}_1, \quad \cdots, \quad \boldsymbol{x}_{n_s}\ \right]^T \tag{8}$$

At the training stage, the model outputs an $n_b \times d_y$ matrix O indicating the prediction value of each bolt. The output matrix O is compared with the ground truth values in the label matrix Y to refine the model.

3.3.2. Encoding sensor-bolt distance and frequency. To take acoustic attenuation into account, the defined adjacency matrix A and feature matrix X need to be further refined according to the physical attenuation model mentioned in section 2.2. The power-law frequency-dependent attenuation model described in equation (3) can be separated into two parts: $e^{-\delta_0 \Delta d}$ for a fixed frequency and $e^{-\omega^\eta}$ for a fixed sensor-bolt distance.

As stated in section 3.1, the graph abstracted from the sensor network and the bolts are almost fully defined by the adjacency matrix A, which is an unweighted graph. To encode the influence of distance to fully define the sensor-bolt layout, a weighted adjacency matrix $\tilde{A}$ is defined as:

$$\tilde{A} = [\tilde{a}_{i,j}]_{n\times n} = \left[a_{i,j} e^{-\delta_0 d_{i,j}}\right]_{n\times n} \tag{9}$$

where $a_{i,j}$ and $\tilde{a}_{i,j}$ are elements of A and $\tilde{A}$ respectively, and $d_{i,j}$ is the distance between node i and node j. For the case of sensor-sensor and bolt-bolt where no connection is established, a large value (10^5) is assigned to $d_{i,j}$.

It should be noted that δ_0 is normally obtained by fitting experimental data, but in this study, we set it as a trainable scalar parameter which is updated in each layer.

On the other hand, the feature matrix X records the CCD of the segmented EMI frequency spectrum and is independent of distance, to compensate for the attenuation effect induced by frequency, a modified feature matrix $\tilde{X}$ is defined as:

$$\tilde{X} = [\widetilde{\boldsymbol{x}_j}]_{1\times d_0} = \left[e^{\bar{\omega}_j^\eta} \boldsymbol{x_j}\right]_{1\times d_0} \tag{10}$$

where $\boldsymbol{x}_j$ and $\widetilde{\boldsymbol{x}}_j$ are $n \times 1$ column vectors of X and $\tilde{X}$ containing features under frequency sub-range $[\omega_j, \omega_{j+1}]$ respectively, and $\bar{\omega}_j$ is the medium frequency of the jth sub-range as a compromise (since there is only one element for each node under each sub-range). According to previous studies [45, 46, 53–55], the coefficient η ranges from 0 to 2. For most metals and crystalline materials where the bolt structure in this study applies, $\eta = 2$.

To prevent $\tilde{A}$ from completely changing the scale of the feature vectors, researchers usually normalize $\tilde{A}$ such that all rows are sum to one. However, this process makes each node independently normalized. Regarding the loosening of multiple bolts jointly influence EMI measurements, we normalize $\tilde{A}$ in matrix level and obtain a $\tilde{A}_{norm}$ ready for the forward propagation in the learning network:

$$\tilde{A}_{\text{norm}} = \tilde{A} \Big/ \left(\frac{1}{n}\sum_{i=1}^{n}\sum_{j=1}^{n}\tilde{a}_{i,j}\right). \tag{11}$$

3.3.3. Forward propagation and training process. Having fully defined the adjacency matrix and the feature matrix concerning the physical background, we can define the forward propagation rule and subsequently establish the whole EMI-GCN model. As introduced in section 3.2, suppose there are l layers in the GCN model. The k^{th} graph convolution layer transforms the output of previous layer $O^{(k-1)}$:

$$\begin{aligned} \tilde{O}^{(k)} &= \tilde{A}_{\text{norm}}{}^{(k)} O^{(k-1)} W^{(k)} + B^{(k)} \\ O^{(k)} &= \text{ReLU}\left(\tilde{O}^{(k)}\right) \end{aligned} \tag{12}$$

where $A^{(k)}$ is controlled by $\sigma^{(k)}$; $W^{(k)}$ is an $d_{k-1} \times d_k$ matrix that contains learnable weights and gradually shrinks the size of feature; $B^{(k)}$ means the bias and ReLU (rectified linear unit) is a type of activation function that induces non-linearity. Mathematically, ReLU elementwise conducts $y = \max(0, x)$.

In the output layer, only the bolt nodes are concerned, so the adjacency matrix $\text{A}^{(l)}$ is:

$$\tilde{A}_{\text{norm}}{}^{(l)} = [\widetilde{\boldsymbol{a}}_{i,j}]_{n_b\times n} = \left[e^{-\delta_0{}^{(l)} \boldsymbol{d}_{i,j}}\right]_{n_b\times n}. \tag{13}$$

The activation function is abandoned:

$$\tilde{O}^{(l)} = \tilde{A}^{(l)}_{\text{norm}} O^{(l-1)} W^{(l)} + B^{(l)}. \tag{14}$$

Basically, the model aims to learn three things:

- The distance between locations of bolts of interest and locations of sensors is different, so the GCN needs to handle the sensitivity of impedance changes to bolt changes. This information is encoded in the parameter δ_0.
- Since the features are input directly without manual selection. The GCN needs to identify the frequency range that is sensitive to the bolt loosening rather than the boundary or environmental conditions. This can be encoded in parameters in W.
- The impedance changes are simultaneously influenced by several bolts (two in this case), so the GCN needs to distinguish the effect of the changes of two bolts. Each node can repeatedly receive and send the information from and to its distant neighbors. In this process, the mixture is gradually and implicitly separated.

Figure 6 describes the full process of the EMI-GCN model. The segmented feature matrix is plotted in gradient colors representing low frequency to high frequency.

In terms of the training process, for a graph, only the output values of the bolt nodes are accounted in the cost function:

$$J = \frac{1}{2n_b}\left\|\tilde{O}^{(l)} - Y\right\|_2^2 \tag{15}$$

where Y and $\tilde{O}^{(l)}$ are the label matrix (torque loss) and the output of the model for bolt nodes, both of which are $n_\text{b} \times d_y$. In this Equation, the cost J is a scalar measured by mean square error (MSE).

The partial derivative of cost function with respect to each parameter (the gradient) can be derived based on the chain rule:

$$\frac{\partial J}{\partial \tilde{O}^{(l)}} = \frac{1}{n_b}\left(\tilde{O}^{(l)} - Y\right). \tag{16}$$

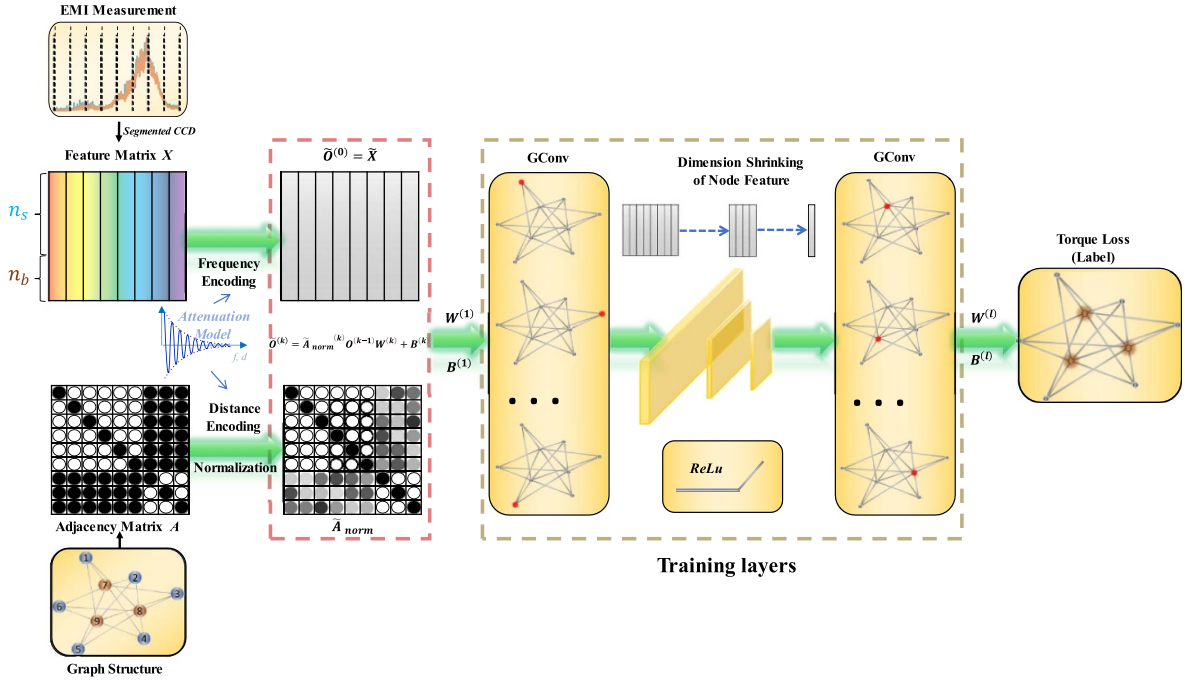

Figure 6. Procedures of EMI-GCN model.

For kth layer, the partial derivative with respect to ${\delta_0}^{(k)}$, $W^{(k)}$ and $B^{(k)}$ are:

$$\begin{aligned}
\frac{\partial J}{\partial A^{(k)}} &= \frac{\partial J}{\partial \tilde{O}^{(k)}}\left[X^{(k-1)}W^{(k)}\right]^T \\
\frac{\partial J}{\partial \tilde{A}^{(k)}} &= \frac{\partial J}{\partial A^{(k)}} \Big/ \left(\frac{1}{n}\sum_{i=1}^{n}\sum_{j=1}^{n}\tilde{a}_{i,j}^{(k)}\right) \\
\frac{\partial J}{\partial {\delta_0}^{(k)}} &= \left[-d_{j,i} \times e^{-{\delta_0}^{(k)} d_{i,j}}\right]_{n\times n} \times \frac{\partial J}{\partial \tilde{A}^{(k)}} \\
\frac{\partial J}{\partial W^{(k)}} &= \left[A^{(k)}X^{(k-1)}\right]^T \frac{\partial J}{\partial \tilde{O}^{(k)}} \\
\frac{\partial J}{\partial B^{(k)}} &= \frac{\partial J}{\partial \tilde{O}^{(k)}}.
\end{aligned} \tag{17}$$

The gradient can be propagated from k to the $k-1$ layer:

$$\begin{aligned}
\frac{\partial J}{\partial O^{(k-1)}} &= \left[A^{(k)}\right]^T \frac{\partial J}{\partial \tilde{O}^{(k)}}\left[W^{(k)}\right]^T \\
\frac{\partial J}{\partial \tilde{O}^{(k-1)}} &= \frac{\partial J}{\partial O^{(k-1)}} I\left[O^{(l-1)} > 0\right].
\end{aligned} \tag{18}$$

After that, the parameters can be updated using gradient descent:

$$\begin{aligned}
\sigma^{(k)} &\leftarrow \sigma^{(k)} - \frac{\partial J}{\partial \sigma^{(k)}} \\
W^{(k)} &\leftarrow W^{(k)} - \eta\frac{\partial J}{\partial W^{(k)}} \\
B^{(k)} &\leftarrow B^{(k)} - \frac{\partial J}{\partial B^{(k)}}
\end{aligned} \tag{19}$$

where η is the learning rate that determines the speed of updating.

4. Proof-of-concept validation

To validate the proposed approach and the EMI-GCN model, a proof-of-concept experiment was conducted in the lab. The test specimen is a pair of 140 × 159 × 10 mm EN24 steel plates connected by two M6 bolts. In practical large-scale applications, fewer sensors are always preferred to optimize the cost-benefit trade-off, and in the lab environment, we wish to obtain more training data from limited test configurations. Therefore, a three-sensor network was adopted for model establishment, and further performance comparison is presented in this section to demonstrate the sufficient necessity of three sensors to form up an efficient sensor network.

4.1. Experimental setup

4.1.1. Implementation of sensor network and data acquisition. As shown in figure 7, 13 PZT sensing patches were randomly implemented on the test specimen. The PZT sensors were divided into two groups with 7 (denoted as Tr1 ∼ Tr7) used for EMI-GCN model training and 6 (denoted as Te1 ∼ Te6) used for model testing. The training group provides $C_7^3 = 35$ sensor network combinations, and the testing group provides $C_6^3 = 20$ sensor network combinations. Sensor-bolt distances were measured with a caliper from the center of each bolt to the center of each sensor and tabulated in table 2. In *in-situ* monitoring scenarios where many bolts might cluster in a small area, to increase measuring efficiency, we plan to measure the coordinates of each bolt and each sensor with respect to the pre-chosen reference point and calculate the sensor-bolt distance according to their coordinates.

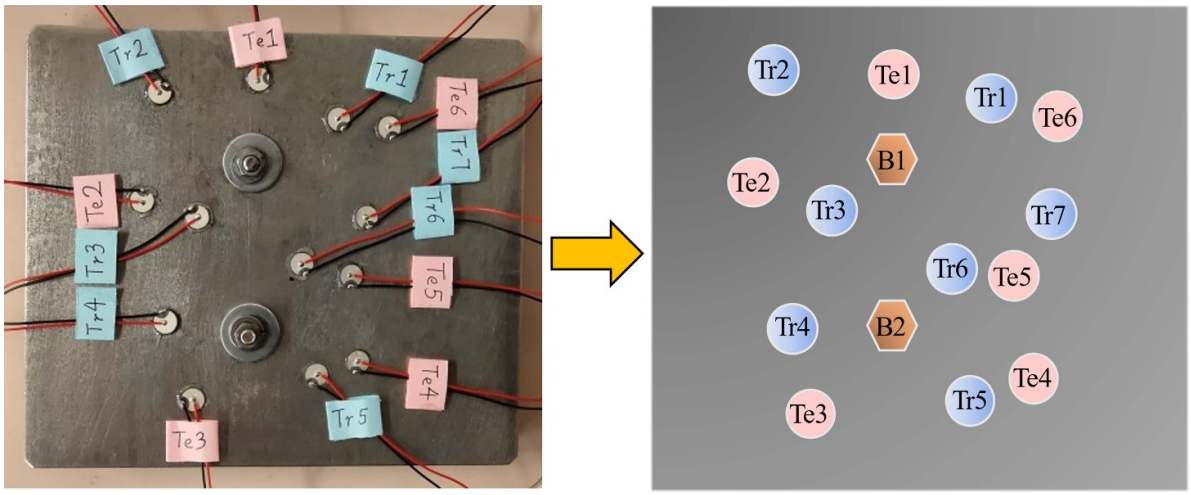

Figure 7. Test specimen and implemented sensors.

Table 2. Distances between sensors and bolts (cm).

	B1	B2
Tr1	3.17	7.38
Tr2	3.83	8.29
Tr3	2.36	4.11
Tr4	5.68	2.63
Tr5	7.11	2.55
Tr6	3.56	2.75
Tr7	4.20	5.41
Te1	2.71	8.07
Te2	3.54	5.35
Te3	7.78	2.66
Te4	7.27	3.67
Te5	4.80	3.89
Te6	4.68	7.98

As shown in figure 8, the specimen was placed on a vibrator that generates stochastic low-amplitude vibrations to simulate a realistic operating environment. An Analog Discovery 2 Logic Analyzer (Digilent Inc., United States) was used to measure the EMI spectrums with a scanning frequency from 100 kHz to 500 kHz (0.1–0.5 MHz) at 1 kHz step. The excitation amplitude was 1 V. Previous studies realized that the temperature effect is significant and used different methods to compensate for it [56–58]. The experiment was taken under a controlled ambient temperature of 25 °C with ±0.5 °C fluctuations so that the influence of temperature is significantly suppressed.

In the training data acquisition stage, a series of residual torques (0 Nm, 1 Nm, 1.5 Nm, 2 Nm, 2.5 Nm, 3 Nm) was applied on each of the bolts from fully loosened state to fully tightened state controlled by a torque wrench, while 3 Nm is the maximum torque we can apply on the bolts based on multiple measurements at fully tightened state. The corresponding torque losses are 3 Nm, 2 Nm, 1.5 Nm, 1 Nm, 0.5 Nm and 0 Nm, respectively. For the two bolted joints there are 36 combinations of load conditions. Therefore, in total 1260 samples can be obtained for training and model selection.

In terms of the testing stage, the same series of torques were applied to each of the two bolts providing 36 loading combinations. Although the applied torque series are the same in the training and testing stages, it should be noted that the training data and testing data samples are completely different, as the sensor implementations, i.e. the sensor network are totally different. In total there are 720 samples for testing, which are totally unseen case by the well-trained model. In this way, the generalization capability and flexibility of our approach can be proved.

It should be admitted that the residual torques measured by a torque wrench do not precisely reflect the realistic situation, i.e. the ground truth is not literally 'true', and therefore altering the model predictions correspondingly. However, it is obvious that such error is a relative term and does not influence the validation result, because the situation is identical at both the training stage and testing stage.

Three EMI measurements were taken and averaged for each sensor under each bolt combination. As mentioned in section 3, only the real part is considered in this study. Figure 9 shows several examples of the EMI measurements (real part). (Sensor Tr1, Tr4, Tr7; Bolt B1, B2 (0,0), (1,2), (2.5,1), (3,3)).

According to section 3.1, for any three-sensor network combined with the two bolts, a five-node graph and a unique adjacency matrix can be defined, as shown in figure 10.

The EMI-GCN model was trained with the 1260 training samples following the process in figure 6, and they were divided into three datasets, as listed in table 3. Each sample is a graph that contains features and labels.

4.1.2. Training details and model selection. The training, validating and testing process was conducted on a workstation with an Intel(R) Core(TM) i7-6700 3.4 GHz processor, 16GB RAM, and an Nvidia RTX2070 Graphic Card.

In this work, batch gradient descent was performed. In other words, for each training iteration, the model ingested all the samples in the training set, calculated the cost function, conducted backpropagation and updated the parameters.

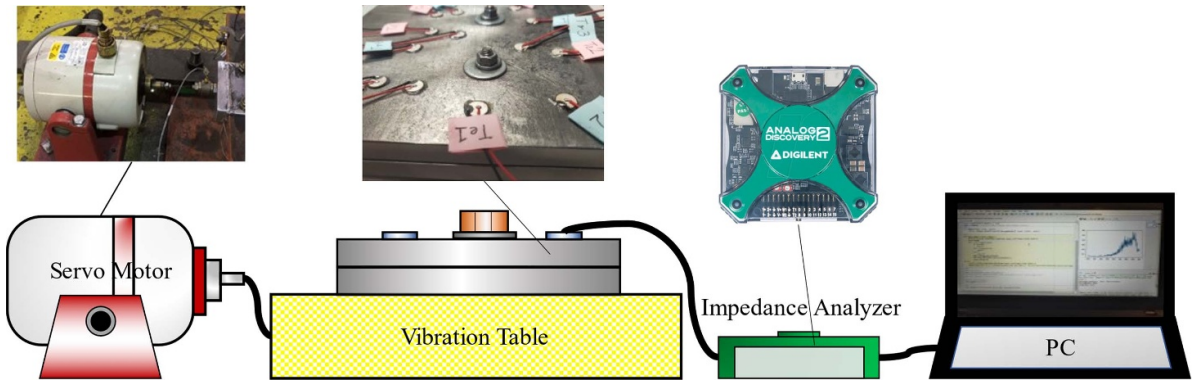

Figure 8. Validation test setup.

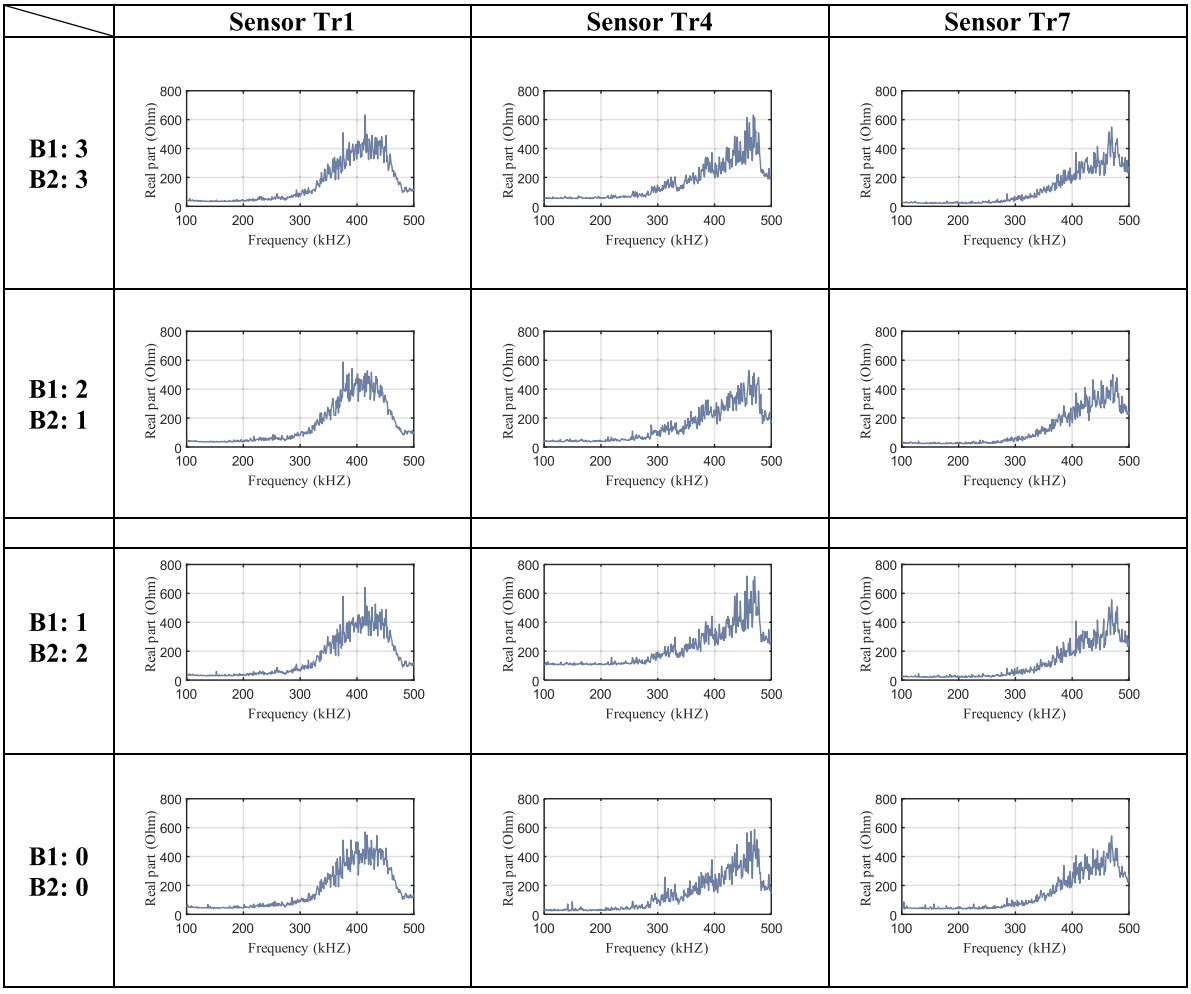

Figure 9. Real component of impedance measurements of different sensors for different conditions.

Adam [59] was used as the optimizer, and dropout [60] was used to prevent overfitting by inducing stochasticity. In this study, the tunable hyperparameters include:

- The learning rate (10^{-3}, 10^{-4});
- The number of sub-frequency range (8, 16, 25);
- The number of layers (2, 3);
- The size of hidden layer (gradually shrinking depending on the number of layers).

To select the hyperparameters for training the model properly rather than arbitrarily, an extra development set is randomly cropped out from the available samples (as shown in table 3). After that, a pool of models with different settings

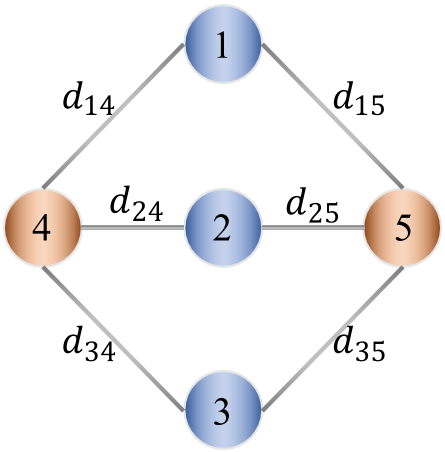

Figure 10. One graph encoding nodes.

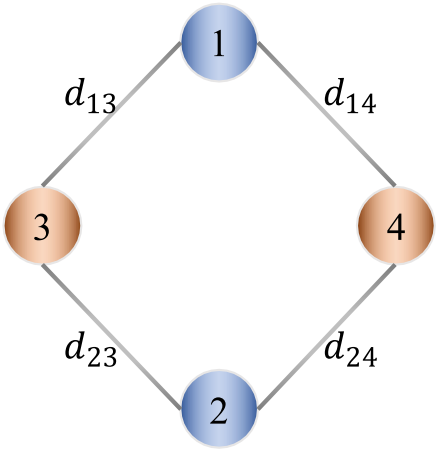

Figure 11. One graph encoding nodes for EMI-GCN-light.

Table 3. Size of datasets.

Dataset type	Size
Training	1008
Development set (for model selection)	252
Testing	720
Total	1980

(hyper-parameters) was developed based on the same training set, which was then evaluated on the development set by mean absolute error (MAE). Based on the performance, the GCN model with the highest MAE on the development set was selected. Given final prediction $\tilde{O}^{(l)}$ and the true torque loss Y, the MSE is calculated by

$$\mathrm{MAE} = \frac{1}{n_b}\left\|\tilde{O}^{(l)} - Y_1\right\|. \tag{20}$$

After model selection, the number of sub-frequency range is set as 25. In other words, the CCD is calculated for every range of 16 kHz. The model has two hidden layers with sizes of 16 and 9, respectively. The influence of the learning rate is trivial and is set as 10^{-3}.

4.2. Baseline models

Three baseline models were developed for comparison to prove the superiority of our approach. To ensure fairness, all models were tuned on the same development dataset to find the optimal settings and tested on the testing dataset.

The first baseline model adopts two sensors to form up a four-node graph with the bolts. The graph for this model is illustrated in figure 11. As a light version of EMI-GCN, it is noted as EMI-GCN-Light. In this case, there are 756 ($C_7^2 \times 6^2$) samples for training and development, and 540 ($C_7^2 \times 6^2$) cases for testing.

Baseline model 2 (noted as GCN-Naïve) ignores the acoustic attenuation of EMI, i.e. the influence of distance and frequency, by directly using the unweighted adjacency matrix and the original feature matrix. Specifically, the adjacency matrix follows equation (4), the feature matrix follows equation (8) and the forward propagation follows equation (6).

Baseline model 3 is a conventional CNN model that incorporates the distances in the prediction of torque loss, denoted as EMI-CNN. This process is shown in figure 12. First of all, the EMI-CNN learns a branch of filters to extract high-level features from the CC vector. It should be noted that each sensor shared the same branch of filters and the operation can thus be considered convolution on the feature matrix. The process gradually shrinks the dimension of feature for each sensor. The features are then concatenated to the distance vector and fed to a multi-layer perception, which learns to account for both impedance measurements and distances between the sensors and bolts and output the value of bolt looseness.

4.3. Sensitivity of CCD for bolt loosening

Before presenting the performance of the EMI-GCN model, we conducted a pilot analysis to show the effectiveness of CCD on indicating bolt looseness as well as to emphasize the need for GCN and sensor network on multiple bolt monitoring. The curve of impedance signature is divided into five sections. For each section, the CCD is calculated using equation (7). The results are shown in figure 13.

In the case shown in figure 13(a), bolt B2 was fixed, and bolt B1 was gradually loosened. The CCD of Tr1 is investigated, since this sensor is close to bolt B1. It can be seen that the CCD increases as the torque loss rises in every frequency section, which means that the signatures become less correlated to the reference signature. The first and second sections (i.e. 100–180 kHz and 180–260 kHz) were found to be more sensitive than the others. A similar phenomenon can be observed in figure 13(b) when bolt B1 was kept fixed, and bolt B2 gradually loosened. The various scale may be ascribed to different boundary conditions as the PZT elements were implemented at different locations of the host structure. It is, therefore, demonstrated that the selected statistic metric can

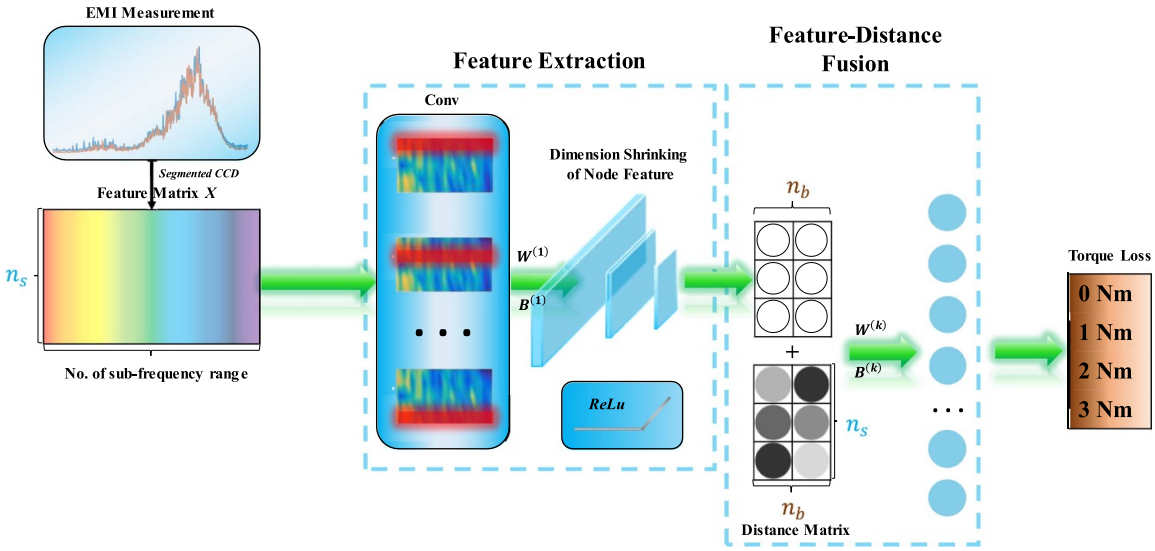

Figure 12. Procedures of EMI-CNN model.

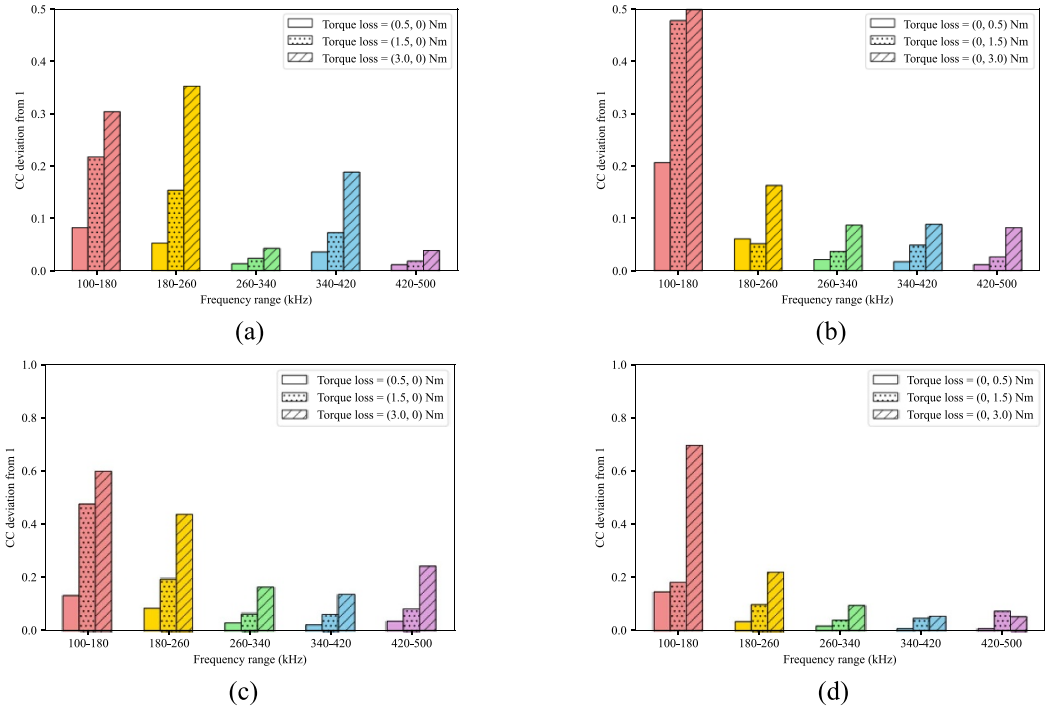

Figure 13. CCD vs torque loss: (a) sensor Tr1 with bolt B1 loosening; (b) sensor Tr4 with bolt B2 loosening; (c) sensor Tr7 with bolt B1 loosening; (d) sensor Tr7 with bolt B2 loosening.

well indicate the torque loss of a single bolt when the other conditions are well controlled.

However, it should be noted that single-bolt monitoring is a forward process, i.e. we already know how much a bolt is loosened (the cause) and use it to explain the metric deviation (the phenomenon). In a multiple-bolt situation, loosening occurred on any of the bolts may induce undistinguishable influence on a sensor when the bolts are approximately equidistant to the sensor, as shown in figures 13(c) and (d) where the sensor-bolt distance of Tr7–B1 and Tr7–B2 are close to each other. In addition, when multiple bolts are loosened, it becomes an inverse problem to figure out the weighted contributions on a sensor and cannot be solved by simply looking at the CCDs, which is why the EMI-GCN is needed.

4.4. Results and comparisons

4.4.1. Performance of EMI-GCN compared with baselines. The EMI-GCN was trained on the data collected and selected on the development set, as described in section 4.1. The performance of the selected model was evaluated on the testing dataset, which has been totally unseen in the training stage. In our case, as the architecture of GCN is not large, both the training and the testing are quite efficient. Training for 1000

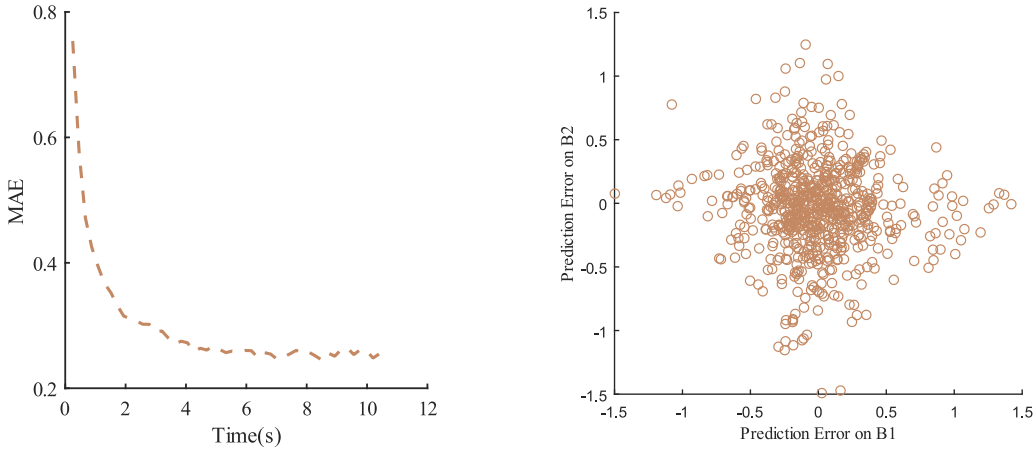

Figure 14. (a) MAE decay on training; (b) prediction errors on all testing samples using EMI-GCN.

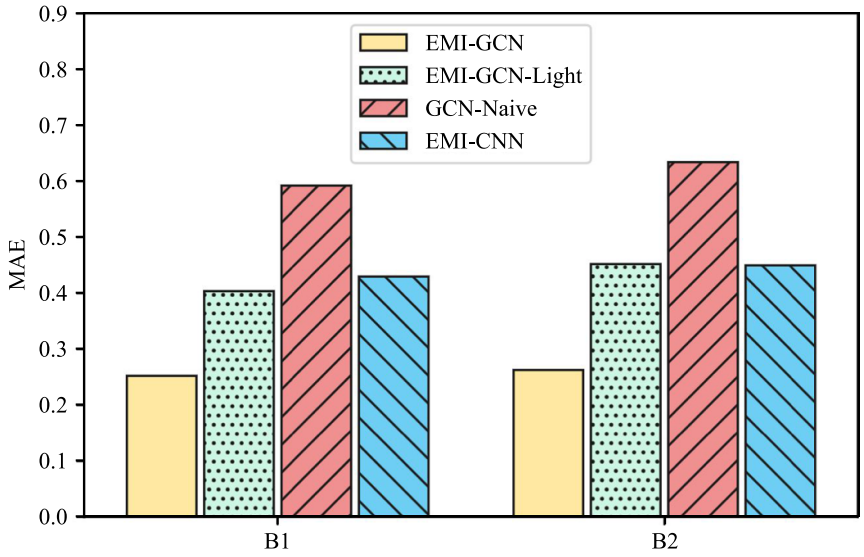

Figure 15. Comparison between EMI-GCN and baseline models.

iterations takes less than 10 s while the testing can be completed instantly. As shown in figure 14(a), the MAE quickly decays to around 0.25 within in 5 s. This high efficiency is desired in real practice.

On all testing samples, the MAE of predicting torque loss is 0.258 N m (0.253 N m for bolt 1 and 0.263 N m for bolt B), accounting for 8.6% of the variation range 0–3 N m. Figure 14(b) shows the prediction errors of all testing samples using EMI-GCN. It can be noted most of the errors are within $\pm$0.5 N m. This error may be ascribed to the inevitable manipulation difference every time we tighten and loosen the bolts manually. In view that the flexibility of sensor arrangement, the results are quite acceptable.

The performances of three baseline models are evaluated on the testing dataset in terms of the MAE level and compared with the EMI-GCN model, as shown in figure 15. The MAEs of three baseline models are 0.43, 0.62 and 0.44 respectively. It can be observed that the average MAE of EMI-GCN model (0.26) is significantly lower than that of three baseline models (0.43, 0.62 and 0.44 respectively). Due to the decrease of sensor numbers, the EMI-GCN-Light model performs worse than the proposed model as expected. However, it does not mean the performance is monotonically improving with respect to increasing sensing nodes, and this will be further discussed in the following subsections. The EMI-CNN model considers sensor-bolt distance, although in a relatively sloppy way, and therefore performs moderately. While GCN-Naïve without sensor-bolt distance encoded exhibits worst performances among all four models, indicating that if the sensor-bolt distance is not considered, forcibly using GCN might instead hinder the torque loss determination.

To get more specific and straightforward impressions on the performance of the proposed model, two examples using EMI-GCN are illustrated in figure 16. Sensor-bolt distances were measured, as displayed on the edges. Based on the measured EMI signatures including reference data under fully tightened condition, CCDs were obtained, as shown in the red blocks. Finally, the consisted feature matrix, as well as the distances, are input to the well-developed EMI-GCN model,

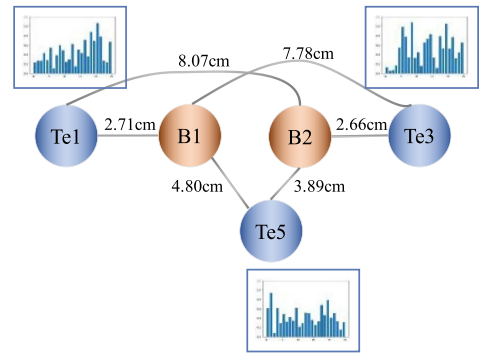

Bolt	Truth (Loss)	Predicted (Loss)
B1	1Nm	0.92Nm
B2	2Nm	2.06Nm

(a)

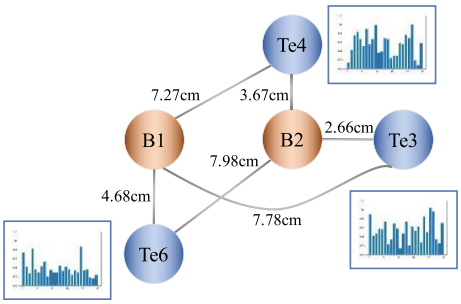

Bolt	Truth (Loss)	Predicted (Loss)
B1	0.5Nm	0.59Nm
B2	3Nm	2.97Nm

(b)

Figure 16. Examples of EMI-GCN making predictions.

which delivers predictions on the torque loss. The results are shown in the table with an MAE of 0.07 N m.

To further understand how information is transmitted and processed in the EMI-GCN structure to achieve our targets, the capability of the EMI-GCN model is further elaborated in the following three subsections based on the experimental validation results, in correspondence to the three targets proposed in section 3.3.3,

4.4.2. Transmission of sensor-bolt distance information. As mentioned in section 3.3.2, we encoded the sensor-bolt distance in the weighted adjacency matrix. Since the δ_0 has been obtained at the training stage, we can now calculate the weighted adjacency matrix and see how information is transmitted between sensors and bolts. Figure 17 shows how the transformed features are distributed between sensors and bolts in the first graph convolution layer. Taking two sensor network examples as shown in figures 17(a) and (d), the further a sensor is from the bolt, the less CCD it will be distributed (figures 17(b) and (e)).

By contrast, baseline model 2 uses an unweighted adjacency matrix. As shown in figures 17(c) and (f), the bolt will evenly receive information from each of the sensors, which is not meaningful. The loss of distance information corrupts the performance: the MSE sharply rises to 0.61. This well demonstrates the importance of taking distance into account.

Although the distance factor is considered, the EMI-CNN (baseline 3), still performs worse than EMI-GCN. We attribute it to the separation of feature extraction and distance consideration. As shown in figure 12, the model does not leverage the distance information until the very last moment, which lowers the performance.

4.4.3. Selection of sensitive frequency sub-range. Figure 18 shows the weight matrix of the first GCN layer and the second GCN layer. The first layer transforms 25 CCDs into 16 features for each node while the second layer transforms 16 features into 9 features.

To identity the importance of each feature, i.e. the frequency range that is sensitive to the bolt looseness but not sensitive to the boundary conditions, we calculated the permutation feature importance for each frequency range.

Permutation feature importance is a model inspection technique when the data is tabulated. The permutation feature importance is defined to be the decrease in a model score when a single feature value is randomly shuffled [61]. This procedure breaks the relationship between the feature and the target, thus the drop in the model score is indicative of how much the model depends on the feature. If the permutation of one feature does not influence the result at all, this feature (CCD of a specific frequency range) must be insignificant.

In our case, the feature matrix set D is tabulated with shape (720, 5, 25) and the MAE on 720 testing samples is 0.2578. The procedure is summarized in table 4.

The results are shown in figure 19. The most bolt loose-sensitive four ranges are 484–500 kHz, 388–404 kHz, 148–154 kHz as well as 228–244 kHz. The corresponding increases in error are 0.441, 0.371. 0.337 and 0.317, respectively.

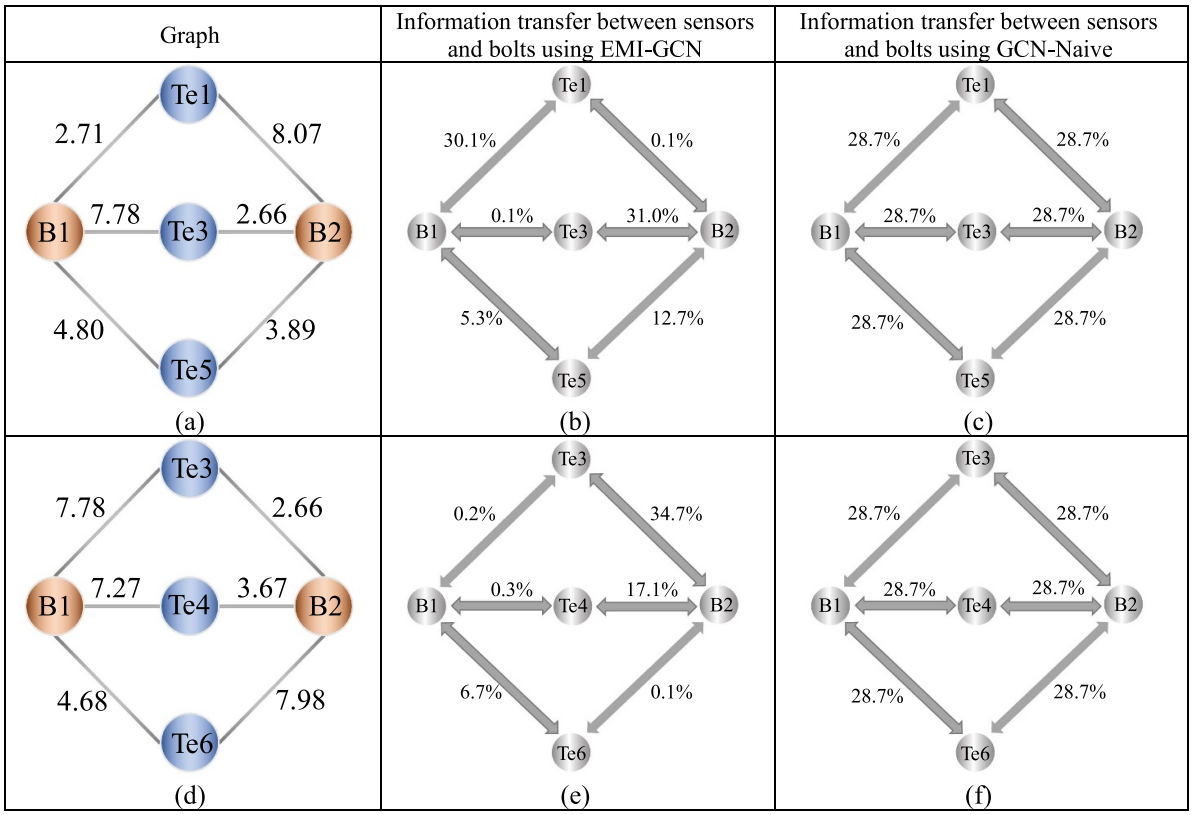

Figure 17. Information transfer between sensor nodes and bolt nodes.

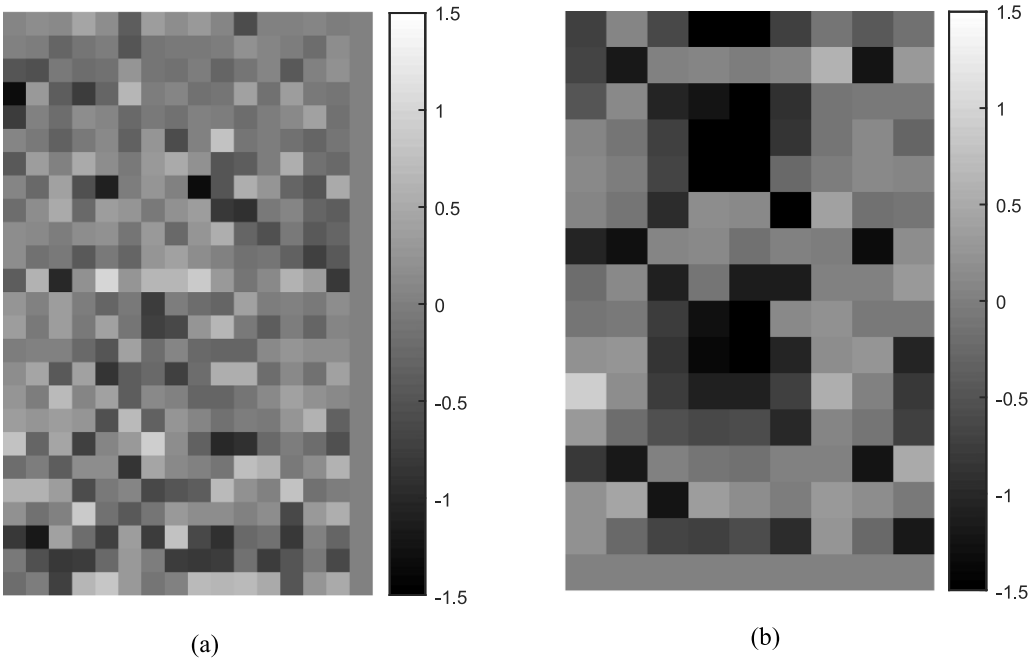

Figure 18. The learned weight of EMI-GCN: (a) the first hidden layer; (b) the second hidden layer.

4.4.4. Distinguishment of multiple bolts with proper sensor network size. In the validation experiment, we presumably adopted a three-sensor network to monitor the looseness of two bolts. The number of information sources is slightly larger than the number of variation sources. In this way, the underdetermined problem can be avoided when we are solving the inverse problem.

We further investigated the influence of network size. Similar to the baseline model EMI-GCN-Light, we also utilized a sensor network using four sensors and the corresponding GCN

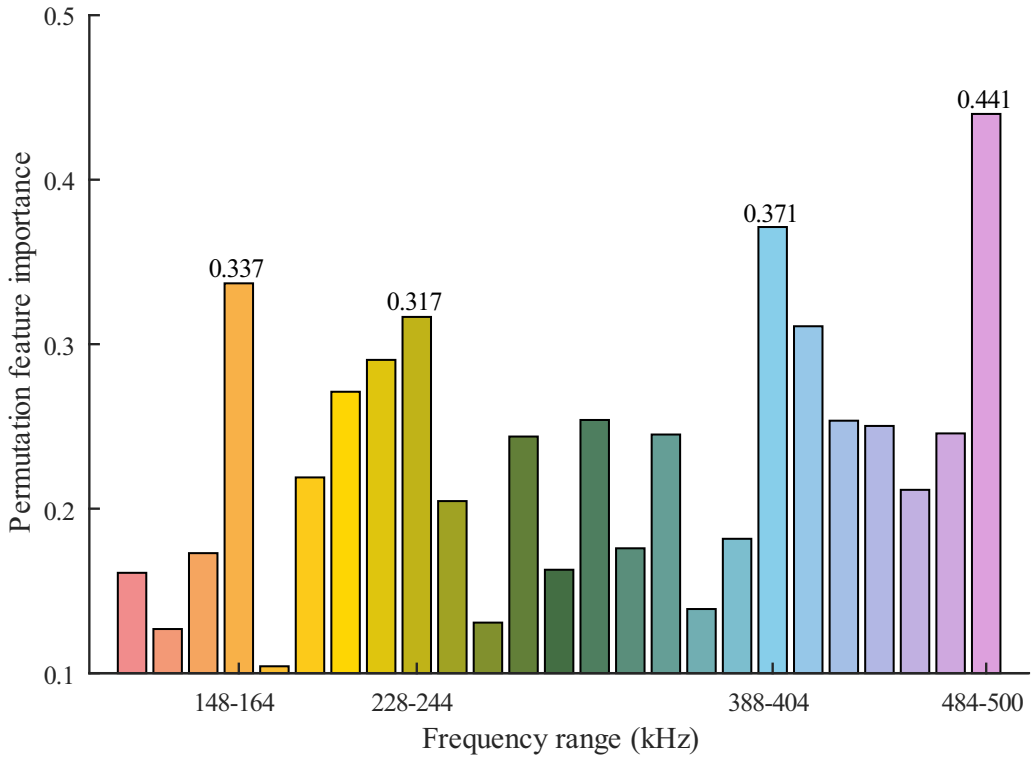

Figure 19. Permutation feature importance of each frequency range.

Table 4. Procedures for calculate feature importance.

For each feature j (3rd dimension of D):
For each repetition k in 1, 2, …, 30:
- Randomly shuffle the 1st dimension of D to generate the corrupted version of the feature set D'
- Input D' to the EMI-GCN model to calculate $\mathrm{MAE_{j,k}}$

Compute the importance of this feature $I_j = \frac{1}{30}\sum_{1}^{30}\mathrm{MAE}_{j,k} - \mathrm{MAE}$

model is denoted as EMI-GCN-Heavy. The training and development set consists of 1260 samples while the testing set consists of 540 samples.

Table 5 shows the performance of these three models on both their training set and testing set. On one hand, in the training set, it is found that the larger the model, the smaller the prediction error. This phenomenon reveals that the reduction of sensors interrupts the accuracy because two sensors cannot distinguish the components in impedance signatures influenced by different bolts as well as three sensors can do. On the other hand, the performance of the EMI-GCN-Heavy is less satisfactory on the testing set because of overfitting. This model with large capacity may fit some noises such as EMI variations induced by temperature change or boundary condition, while the 1260 samples are not adequate to help to separate these factors of variation. As a result, the model fails to generalize to the new conditions.

To summarize, the size of sensor network should match the number of variation sources. An undersized network may fail to detect or distinguish different variations while an oversized network may encounter an overfitting problem once the training samples are not adequate.

Table 5. Influence of network size on MSE on training and testing set.

Model	Sensor network size	MAE on training set	MAE on testing set
EMI-GCN-Light	2	0.366	0.428
EMI-GCN	3	0.237	0.258
EMI-GCN-Heavy	4	0.206	0.378

5. Conclusions and future work

In this study, a novel EMI-based approach for monitoring looseness of clustered bolted joints is proposed, by implementing a PZT sensor network and establishing a hybrid EMI-GCN model. The EMI-GCN model incorporates both physical acoustic attenuation nature and data-driven analysis, with the GCN model retaining the graph structure abstracted from the sensor network and the clustered bolted joints, and the physical model reflecting the influence of sensor-bolt distance and

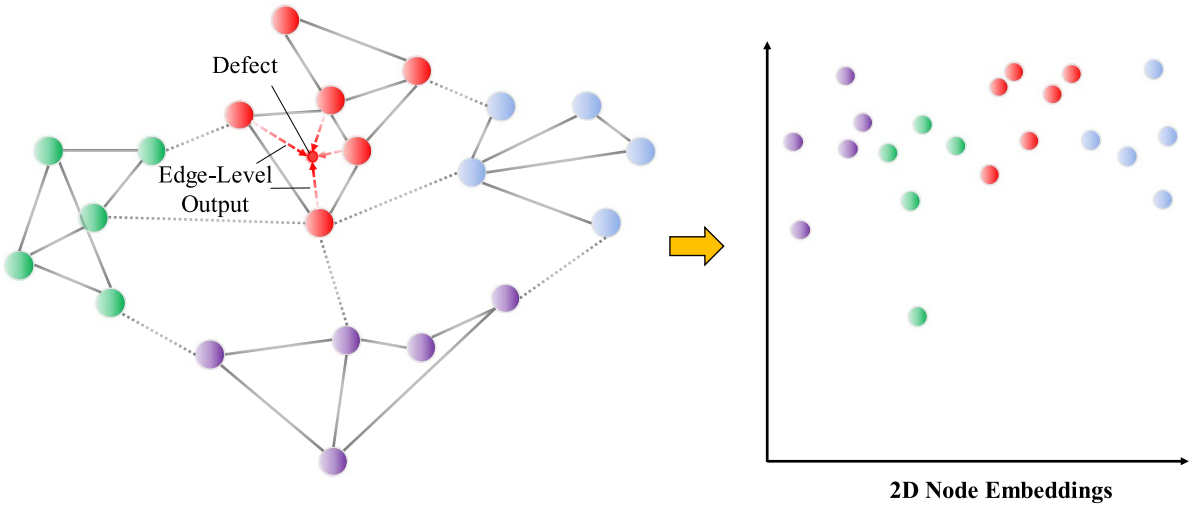

Figure 20. Damage localization with a large sensor network.

sweeping frequency on EMI sensing. A series of model selections were carried out to finetune the hyperparameters (division numbers of sub-frequency range, etc) of the established model. The proof-of-concept experiment showed that the proposed approach outperforms all three baseline models in terms of both capability and prediction accuracy, demonstrating its effectiveness as well as superiority. In comparison to other EMI-based monitoring methods, the proposed approach bears the following merits:

- As a senor network, it can monitor the state and provide quantified torque losses for multiple bolted joints simultaneously, while most existing EMI-based monitoring methods follow one sensor to one bolt configuration;
- By encoding sensor-bolt distance into the GCN model, the influence of each bolt state variation on a sensor can be thoroughly and distinguishably revealed through the training process, thus offering more accurate torque loss predictions than normal GCNs and other ML algorithms;
- The EMI-GCN model can provide regressive predictions using limited training data, in terms of torque loss and more importantly, sensor network combinations. This is particularly useful for real applications where it is tricky and impractical to guarantee a consistent sensor placement strategy with those networks for training. It allows a more flexible implementation strategy as long as the sensors are within the effective sensing range.

Apart from the above merits, the proposed EMI-GCN model can select the frequency ranges that are sensitive to the bolt loosening while insensitive to the environmental variations. Finally, we showed that the size of sensor network should match the number of variation sources. An undersized model (EMI-GCN-Light) may fail to detect or distinguish different variations while an oversized network may suffer from the overfitting problem.

To the authors' knowledge, it is for the first time GCN is introduced into the realm of SHM, and we are extending our investigations to further exploit its potential beyond the scenario of EMI-based monitoring: (a). Although we have suppressed the influence of temperature in this study, the temperature is still one of the top concerns in EMI-based monitoring, especially in *in-situ* monitoring scenarios. In future work, we are planning to feed temperature with a learnable parameter into our GCN model, analogous to sensor-bolt distance encoding; (b). In this study we are focusing on bolt loosening cases in which the position of structural variation is pre-known, and only node-level output is delivered from the EMI-GCN model. For more general damage detection scenarios where damage positions are unknown, an enhanced model is preferred to deliver both node-level and edge-level outputs. The damage position can be inferred from the information of neighboring edges in a probability manner. Besides, a general inductive framework GraphSAGE [62] that can efficiently generate node embeddings for previously unseen nodes can be utilized, so that the developed model can handle a graph with varying sizes, i.e. knowledge obtained from one graph can be transferred to graphs with a different number of nodes; c). Although in this study the GCN model is applied on a relatively simple sensor network, its value should be fully utilized in complicated sensor networks implemented in large civil infrastructures and transportation tools. Possible thinking is that considering a sensor network shown in figure 20, a hierarchical GCN model can be proposed by firstly identifying the defect-close region and its neighboring sub-network through 2D node embedding, and defect severity and position can be located through node-level and edge-level outputs.

Acknowledgments

This research was funded by a grant (RIF) from the Research Grants Council of the Hong Kong Special Administrative Region, China, Grant No. R5020-18. This research was also funded by the grants from the Ministry of Science and Technology of China and the Innovation and Technology Commission of Hong Kong SAR Government to the Hong Kong Branch of Chinese National Rail Transit Electrification and

Automation Engineering Technology Research Center, Grant No. K-BBY1.

ORCID iDs

Lu Zhou https://orcid.org/0000-0002-3639-9514
Si-Xin Chen https://orcid.org/0000-0002-1561-0851
Yi-Qing Ni https://orcid.org/0000-0003-1527-7777

References

[1] Gray P J and McCarthy C T 2010 A global bolted joint model for finite element analysis of load distributions in multi-bolt composite joints *Composites* B **41** 317–25
[2] Huo L, Wang F, Li H and Song G 2017 A fractal contact theory based model for bolted connection looseness monitoring using piezoceramic transducers *Smart Mater. Struct.* **26** 104010
[3] Meyer J J and Adams D E 2015 Theoretical and experimental evidence for using impact modulation to assess bolted joints *Nonlinear Dyn.* **81** 103–17
[4] Wang F, Ho S C M and Song G 2019 Modeling and analysis of an impact-acoustic method for bolt looseness identification *Mech. Syst. Signal Process.* **133** 106249
[5] He K and Zhu W D 2014 Detecting loosening of bolted connections in a pipeline using changes in natural frequencies *J. Vib. Acoust.* **136** 034503
[6] Chen S, Zhou L, Ni Y Q and Liu X-Z 2020 An acoustic-homologous transfer learning approach for AE-based rail condition evaluation *Struct. Heal Monit.* 1475921720976941
[7] Huda F, Kajiwara I, Hosoya N and Kawamura S 2013 Bolt loosening analysis and diagnosis by non-contact laser excitation vibration tests *Mech. Syst. Signal Process.* **40** 589–604
[8] Shin H-J, Lee J R and Park C Y 2014 A novel fiber optic bolt loosening monitoring sensor system for aircraft bolt joints *J. Intell. Mater. Syst. Struct.* **25** 647–53
[9] Du F, Xu C, Wu G and Zhang J 2018 Preload monitoring of bolted L-shaped lap joints using virtual time reversal method *Sensors* **18** 1928
[10] Zhang Z, Liu M, Su Z and Xiao Y 2016 Quantitative evaluation of residual torque of a loose bolt based on wave energy dissipation and vibro-acoustic modulation: a comparative study *J. Sound Vib.* **383** 156–70
[11] Zhou L, Brunskill H P and Lewis R 2019 Real-time non-invasive measurement and monitoring of wheel–rail contact using ultrasonic reflectometry *Struct. Health Monit.* **18** 1953–65
[12] Zhou L, Brunskill H, Pletz M, Daves W, Scheriau S and Lewis R 2019 Real-time measurement of dynamic wheel-rail contacts using ultrasonic reflectometry *J. Tribol.* **141** 061401
[13] Ta D, Wang W, Wang Y, Le L H and Zhou Y 2009 Measurement of the dispersion and attenuation of cylindrical ultrasonic guided waves in long bone *Ultrasound Med. Biol.* **35** 641–52
[14] Wang S, Lederman A, Gomez F, Spencer B F and Smith M 2019 Low-cost electromechanical impedance testing damage detection of submerged civil structures *12th Int. Workshop on Structural Health Monitoring* (DEStech Publications Inc.) pp 647–54
[15] Gulizzi V, Rizzo P, Milazzo A and Ribolla E L M 2015 An integrated structural health monitoring system based on electromechanical impedance and guided ultrasonic waves *J. Civ. Struct. Heal Monit.* **5** 337–52
[16] Na W and Baek J 2018 A review of the piezoelectric electromechanical impedance based structural health monitoring technique for engineering structures *Sensors* **18** 1307
[17] Djemana M, Hrairi M, Al Jeroudi Y and Hrairi B M 2017 Using electromechanical impedance and extreme learning machine to detect and locate damage in structures *J. Nondestruct. Eval.* **36** 39
[18] Gao D, Wu Z, Yang L and Zheng Y 2018 Integrated impedance and lamb wave–based structural health monitoring strategy for long-term cycle-loaded composite structure *Struct. Health Monit.* **17** 763–76
[19] de Oliveira M A and Inman D J 2017 Performance analysis of simplified fuzzy ARTMAP and probabilistic neural networks for identifying structural damage growth *Appl. Soft Comput.* **52** 53–63
[20] Zhu X, Di L and Scalea F 2016 Sensitivity to axial stress of electro-mechanical impedance measurements *Exp. Mech.* **56** 1599–610
[21] Zhu J, Wang Y and Qing X 2019 Modified electromechanical impedance-based disbond monitoring for honeycomb sandwich composite structure *Compos. Struct.* **217** 175–85
[22] Malinowski P, Wandowski T and Ostachowicz W 2015 The use of electromechanical impedance conductance signatures for detection of weak adhesive bonds of carbon fibre–reinforced polymer *Struct. Health Monit.* **14** 332–44
[23] Huo L, Chen D, Liang Y, Li H, Feng X and Song G 2017 Impedance based bolt pre-load monitoring using piezoceramic smart washer *Smart Mater. Struct.* **26** 057004
[24] Huynh T C, Dang N L and Kim J T 2018 Preload monitoring in bolted connection using piezoelectric-based smart interface *Sensors* **18** 2766
[25] Li W, Wang J, Liu T and Luo M 2020 Electromechanical impedance instrumented circular piezoelectric-metal transducer for corrosion monitoring: modeling and validation *Smart Mater. Struct.* **29** 035008
[26] Wang D, Li Z and Zhu H 2016 A new three-dimensional electromechanical impedance model for an embedded dual-PZT transducer *Smart Mater. Struct.* **25** 75002
[27] Zhu J, Qing X, Liu X and Wang Y 2021 Electromechanical impedance-based damage localization with novel signatures extraction methodology and modified probability-weighted algorithm *Mech. Syst. Signal Process.* **146** 107001
[28] Na W S 2021 Bolt loosening detection using impedance based non-destructive method and probabilistic neural network technique with minimal training data *Eng. Struct.* **226** 111228
[29] de Rezende S W F, de Moura J D R V, Neto R M F, Gallo C A and Steffen V 2020 Convolutional neural network and impedance-based SHM applied to damage detection *Eng. Res. Express* **2** 35031
[30] de Oliveira M A, Monteiro A V and Filho J V 2018 A new structural health monitoring strategy based on PZT sensors and convolutional neural network *Sensors* **18** 2955
[31] Wang F and Song G 2020 1D-TICapsNet: an audio signal processing algorithm for bolt early looseness detection *Struct. Health Monit.* **15** 1475921720976989
[32] Min J, Park S and Yun C-B 2010 Impedance-based structural health monitoring using neural networks for autonomous frequency range selection *Smart Mater. Struct.* **19** 125011
[33] Min J, Park S, Yun C-B, Lee C-G and Lee C 2012 Impedance-based structural health monitoring incorporating neural network technique for identification of damage type and severity *Eng. Struct.* **39** 210–20
[34] Fan X, Li J and Hao H 2018 Impedance resonant frequency sensitivity based structural damage identification with sparse regularization: experimental studies *Smart Mater. Struct.* **28** 15003

[35] Zahedi F and Huang H 2017 Time–frequency analysis of electro-mechanical impedance (EMI) signature for physics-based damage detections using piezoelectric wafer active sensor (PWAS) *Smart Mater. Struct.* **26** 55010
[36] Liang C, Sun F P P and Rogers C A A 1997 Coupled electro-mechanical analysis of adaptive material systems-determination of the actuator power consumption and system energy transfer *J. Intell. Mater. Syst. Struct.* **8** 335–43
[37] Park G, Farrar C R, Rutherford A C and Robertson A N 2006 Piezoelectric active sensor self-diagnostics using electrical admittance measurements *J. Vib. Acoust.* **128** 469–76
[38] Annamdas V G M and Soh C K 2008 Three-dimensional electromechanical impedance model for multiple piezoceramic transducers—structure interaction *J. Aerosp. Eng.* **21** 35–44
[39] Li N, Wang F and Song G 2020 Monitoring of bolt looseness using piezoelectric transducers: three-dimensional numerical modeling with experimental verification *J. Intell. Mater. Syst. Struct.* **31** 911–8
[40] Zhao S, Fan S, Yang J and Kitpornchai S 2020 Numerical and experimental investigation of electro-mechanical impedance based concrete quantitative damage assessment *Smart Mater. Struct.* **29** 055025
[41] Qiu L, Liu B, Yuan S, Su Z and Ren Y 2016 A scanning spatial-wavenumber filter and PZT 2 D cruciform array based on-line damage imaging method of composite structure *Sensors Actuators* A **248** 62–72
[42] Hanfei Z, Shuhao C, Shiwei M, Yu L, Hanyu X, Qingwei X, Yanyan L and Haiyan Z 2020 Multi-sensor network for industrial metal plate structure monitoring via time reversal ultrasonic guided wave *Measurement* **152** 107345
[43] Huo L, Chen D, Kong Q, Li H and Song G 2017 Smart washer—a piezoceramic-based transducer to monitor looseness of bolted connection *Smart Mater. Struct.* **26** 025033
[44] Holm S and Näsholm S P 2011 A causal and fractional all-frequency wave equation for lossy media *J. Acoust. Soc. Am.* **130** 2195–202
[45] Szabo T L and Wu J 2000 A model for longitudinal and shear wave propagation in viscoelastic media *J. Acoust. Soc. Am.* **107** 2437–46
[46] Szabo T L 1994 Time domain wave equations for lossy media obeying a frequency power law *J. Acoust. Soc. Am.* **96** 491–500
[47] Chen W and Holm S 2003 Modified Szabo's wave equation models for lossy media obeying frequency power law *J. Acoust. Soc. Am.* **114** 2570–4
[48] Wu Z, Pan S, Chen F, Long G, Zhang C and Yu P S 2020 A comprehensive survey on graph neural networks *IEEE Trans. Neural Netw. Learn. Syst.* **32** 1–21
[49] Wu L, Sun P, Hong R, Fu Y, Wang X and Wang M 2018 SocialGCN: an efficient graph convolutional network based model for social recommendation *42nd International ACM SIGIR Conference on Research and Development in Information Retrieval* July *21–25, 2019 Paris, France* (http://arxiv.org/abs/1811.02815)
[50] Zhao L, Song Y, Zhang C, Liu Y, Wang P, Lin T, Deng M and Li H 2019 T-gcn: a temporal graph convolutional network for traffic prediction *IEEE Trans. Intell. Transp. Syst.* **21** 3848–58
[51] Fout A, Byrd J, Shariat B and Ben-Hur A 2017 Protein interface prediction using graph convolutional networks *Advances in Neural Information Processing Systems* pp 6530–9 (https://hdl.handle.net/10217/185661)
[52] Bhalla S, Naidu A S K and Soh C K 2003 Influence of structure-actuator interactions and temperature on piezoelectric mechatronic signatures for NDE *Smart Materials, Structures, and Systems* vol 5062, ed S Mohan, B Dattaguru and S Gopalakrishnan (Bellingham: International Society for Optics and Photonics) pp 263
[53] Chen W and Holm S 2004 Fractional laplacian time-space models for linear and nonlinear lossy media exhibiting arbitrary frequency power-law dependency *J. Acoust. Soc. Am.* **115** 1424–30
[54] Carcione J M, Cavallini F, Mainardi F and Hanyga A 2002 Time-domain modeling of constant-Q seismic waves using fractional derivatives *Pure Appl. Geophys.* **159** 1719–36
[55] D'astrous F T and Foster F S 1986 Frequency dependence of ultrasound attenuation and backscatter in breast tissue *Ultrasound Med. Biol.* **12** 795–808
[56] Gianesini B M, Cortez N E, Antunes R A and Vieira Filho J 2020 Method for removing temperature effect in impedance-based structural health monitoring systems using polynomial regression *Struct. Health Monit.* **20** 202–18
[57] Huynh T and Kim J 2018 RBFN-based temperature compensation method for impedance monitoring in prestressed tendon anchorage *Struct. Control Heal. Monit.* **25** e2173
[58] Zhang X, Zhou W and Li H 2019 Electromechanical impedance-based ice detection of stay cables with temperature compensation *Struct. Control Heal. Monit.* **26** e2384
[59] Kingma D P and Ba J 2015 Adam: a method for stochastic optimization *The 3rd International Conference for Learning Representations* M*ay 7–9, 2015, San Diego* (https://arxiv.org/abs/1412.6980)
[60] Srivastava N, Hinton G, Krizhevsky A, Sutskever I and Salakhutdinov R 2014 Dropout: a simple way to prevent neural networks from overfitting *J. Mach. Learn. Res.* **15** 1929–58
[61] Breiman L 2001 Random forests *Mach. Learn.* **45** 5–32
[62] Hamilton W, Ying Z and Leskovec J 2017 Inductive representation learning on large graphs *Advances in Neural Information Processing Systems* pp 1024–34 (https://arxiv.org/abs/1706.02216)